Univerzita Karlova v Praze
Matematicko-fyzikální fakulta

DIPLOMOVÁ PRÁCE

Bc. Ingrid Jurková

Studium faktorů ovlivňujících funkci membránového transportního proteinu MntH bakterie *E.coli*

Fyzikální ústav Univerzity Karlovy
Vedoucí diplomové práce: RNDr. Eva Urbánková, Ph.D.
Studijní program: Fyzika, obor Biofyzika a chemická fyzika

Acknowledgments

I would like to thank my supervisor RNDr. Eva Urbánková, Ph.D. and my consultant RNDr. Roman Chaloupka, Ph.D. from the Institute of Physics of Charles University for their help, support and patience. I also thank Dr. Bernhard Schmitt from the Department of Physiology of the University of Otago for giving me the opportunity to work on his project and gain experience in mathematical modelling. Finally, I would like to thank RNDr. Tomáš Mančal, Ph.D. from the Institute of Physics of Charles University for valuable discussions on the theoretical aspects of my work.

Prohlašuji, že jsem svou diplomovou práci napsala samostatně a výhradně s použitím citovaných pramenů. Souhlasím se zapůjčováním práce.

V Praze dne 17.4.2009 Ingrid Jurková

Study of factors influencing the function of MntH, membrane transport protein of *E. coli*

Název práce: Studium faktorů ovlivňujících funkci membránového transportního proteinu MntH bakterie *E. coli*
Autor: Bc. Ingrid Jurková
Katedra (ústav): Fyzikální ústav Univerzity Karlovy
Vedoucí diplomové práce: RNDr. Eva Urbánková, Ph.D.
e-mail vedoucího: eva.urbankova@mff.cuni.cz
Abstrakt: Protein MntH patřící do rodiny transportérů Nramp hraje důležitou roli nejen v homeostáze železa a manganu, ale i při obraně bakteriálních buněk před imunitní reakcí napadeného hostitele. Tento protein transportuje do buňky dvojmocné kovové ionty v symportu s protony, přičemž stechiometrie tohoto transportu se mění v závislosti na membránovém potenciálu a na extracelulárním *pH*. V první části této práce byl pomocí redistribuční potenciálové sondy diS-C_3(3) zkoumán vliv exprese *MNTH* a transportu dvojmocných iontů přenašečem MntH na membránový potenciál buněk *E. coli*. Zjistili jsme, že buňky exprimující MNTH jsou hyperpolarizovány a jejich membránový potenciál se depolarizuje po přidání některých dvojmocných kovů. Ve druhé části práce jsme se věnovali teoretickému studiu kinetiky membránových přenašečů popsaných čtyř-, šesti- nebo osmistavovým transportním modelem, do něhož byla zavedena závislost všech rychlostních konstant na membránovém potenciálu. Pomocí matematického modelování byla zkoumána závislost toku přenašečem na různých parametrech transportního modelu, jako jsou například membránový potenciál, koncentrace substrátu nebo náboj substrátu či přenašeče. Byly pozorovány některé jevy, popisované i u proteinu MntH (proměnná stechiometrie transportu a její závislost na potenciálu a *pH*). Pro detailnější modelování transportu pomocí osmistavového kinetického schématu by však bylo třeba znát konkrétněji hodnoty jednotlivých kinetických konstant nebo vztahů mezi nimi.
Klíčová slova: kinetika membránového transportu, MntH, *Escherichia coli*, diS-C_3(3)

Title: Study of factors influencing the function of MntH, membrane transport protein of *E. coli*
Author: Bc. Ingrid Jurková
Department: Institute of Physics of Charles University
Supervisor: RNDr. Eva Urbánková, Ph.D.
Supervisor's e-mail address: eva.urbankova@mff.cuni.cz
Abstract: MntH belongs to the Nramp family of transport proteins, and plays an important role not only in homeostasis of iron and manganese, but also in bacterial defence against the immunity response of an infected host cell. MntH co-transports divalent metal ions into the cell together with protons with a stoichiometry dependent on the membrane potential and extracellular *pH*. Using the redistribution potential dye diS-C_3(3), we measured the effects of *MNTH* expression and MntH-mediated metal transport on the cell membrane potential and intracellular *pH*. Cells expressing *MNTH* were found to be hyperpolarised and their membrane potential was depolarised upon the addition of metal ions. In the theoretical part of our work, we explored general four-, six-, and eight-state carrier models that were modified by introducing the voltage dependence of all rate constants. Using mathematical modelling, we simulated the effect of various model parameters (including membrane potential, substrate concentration, and carrier or substrate charge) on substrate influx. We observed some of the transport characteristics described for MntH proteins such as variable symport stoichiometry that is influenced by the membrane potential and *pH*. However, for a more detailed simulation of the eight-state carrier model, more information about kinetic rate constants would be needed.
Keywords: membrane transport kinetics, MntH, *Escherichia coli*, diS-C_3(3)

1 Introduction

Our work studies several aspects of the transport characteristics and kinetics of membrane proteins, ubiquitous enzymes that are essential for cell homeostasis and for the maintenance of life. We focused on the bacterial MntH protein (Manganese transporter H^+-dependent), which is known to mediate symport of divalent metal ions and protons into the cell and to play an important role in bacterial metal homeostasis and virulence. Symport of positively charged ions with H^+ is quite unusual and there are still some controversial points concerning the energetics of MntH-mediated transport. Moreover, it has been shown that, besides active co-transport, uncoupled metal ion leak or proton leak may occur depending on prevailing conditions.

Because I spent four months in the laboratory of Dr. Bernhard Schmitt at the University of Otago and worked under his guidance on numerical modelling of voltage effects on electroneutral transporters, I decided to take advantage of this experience and extended the developed models to electrogenic carrier schemes that provide a simplified description of the MntH transport mechanisms. To explore membrane potential[I] effects on carrier kinetics, voltage dependence of all rate constants was introduced into the carrier models to describe the effect of substrate charge, carrier charge and voltage on various transport steps. Beginning with the simplest case of a four-state electroneutral uniporter and ending up with a considerably more complicated eight-state symporter model that was specially designed to describe transport via the MntH protein [1], we studied the effect of membrane potential, substrate concentration and carrier and substrate charge on membrane transport. Both the six-state and eight-state carrier models can be regarded as simplified models of the MntH transporter. While the six-state scheme is sufficient to describe proton leak that was observed at low *pH* values, the eight-state model includes also the possibility of H^+-uncoupled metal ion leak that was observed for MntH.

It is not straightforward to compare results obtained by mathematical modelling with experimental results. Up to now, measurements of MntH activity are restricted to experiments on living cells without the control (or knowledge) of electrochemical potential gradients of MntH substrates. Particularly, it would be useful to know the cell membrane potential during transport experiments. We did the first attempt to get information (although only qualitative one) about the membrane potential changes caused by the presence of MntH in bacterial cells

[I] Alternatively, we use the term voltage.

and by MntH-mediated metal ion transport. In order to achieve this, potential-sensitive redistribution dye diS-C_3(3) was used. In addition, the feasibility of simultaneous fluorescence measurements using diS-C_3(3) and pHluorin (a mutant of the Green Fluorescent Protein GFP sensitive to internal *pH*) was explored.

My thesis is divided into three main chapters. Chapter 1 serves as a brief introduction to membrane transport, explains the importance of membrane proteins and introduces the four-, six- and eight-state carrier models and their kinetics with an emphasis on voltage effects on carrier transport. Moreover, Chapter 1 introduces the MntH transport protein as a member of a large Nramp protein family, whose members share a remarkable similarity in transport characteristics and protein topology. Next, Chapter 2 describes experimental and theoretical methods used in our work. These include fluorescent spectroscopy using the diS-C_3(3) redistribution dye and pHluorin, and mathematical modelling methods. Results of our experiments and mathematical simulations are presented and discussed in Chapter 3.

1.1 Membrane transport

1.1.1 Transport proteins

Besides simple diffusion, which allows small uncharged polar molecules such as O_2 or CO_2 to freely pass the cellular membrane, all membrane transport processes are mediated by transport proteins. They facilitate the passage of hydrophilic solutes from one side of a biological membrane to another by forming a continuous protein pathway across the membrane. This enables charged and/or polar molecules such as ions, sugars, amino acids, nucleotides and many cell metabolites to pass across the hydrophobic interior of the lipid bilayer [2]. Transport proteins are therefore unconditionally required in all cells for the maintenance of life. They mediate the uptake of essential nutrients as well as the exodus of end products of metabolism and toxic substances, maintain osmotic stability, enable intracellular communication by the release and uptake of signalling molecules, and allow destroying other organisms by releasing toxins or virulence factors ([3] p. 265). The importance of membrane proteins is also demonstrated by the fact that about 10% of all genes in microorganisms encode transport proteins ([3] p. 1).

Transport protein mediated processes can be divided into two groups: facilitated diffusion and active transport ([4] p. 374). Facilitated diffusion is a passive translocation of substrate that always occurs down its electrochemical gradient and therefore requires no energy ([2], [4] p. 329). In contrast to diffusion, active transport involves coupling of

transmembrane movement of a solute with a biochemical reaction, such that its flow may be against its electrochemical potential gradient ([4] p. 329). In primary active transport, movement of solutes is driven by hydrolysis of phosphoric acid anhydride bonds in ATP ([3] p. 49). This provides energy for solute transport against their electrochemical gradient without dissipating gradients of other molecules. Gradients formed through primary active transport can be further utilized to perform other work, such as to produce physical or electrical changes in the cell or to produce and maintain gradients of other solutes ([3] p. 40 and p. 117). Secondary active transporters derive energy from such solute gradients and use it for transport of another solute against its concentration gradient [5]. In this way, uphill transport of one solute across the membrane is coupled to the downhill transport of another molecule [2].

Membrane proteins are historically divided into membrane channels and carriers according to their structure and transport mechanism ([3] p. 239). However, channel and carrier models should not be regarded as mutually exclusive possibilities but rather as limiting cases of a more general transport mechanism [6]. Channel proteins form selective pores across the membrane that can be further regulated by phosphorylation or by gating in response to ligands or changes in the electrical membrane potential ([3] p. 239, [5]). During their transport cycle, channels undergo only very small changes in their conformation ([3] p. 239). The turnover number of a channel, defined as the maximum number of molecules that may pass through a transport pathway per second, is in the order of 10^6 sec^{-1}. Carrier proteins, on the other hand, have a turnover number from about 1 sec^{-1} to 10^5 sec^{-1} because their interaction with solutes is much stronger ([3] p. 65). Carriers bind the specific solute to be transported and undergo a series of conformational changes that allow transferring the bound solute from one side of the membrane to another ([2], [3] p. 239). They are usually regulated more slowly than channel proteins ([3] p. 65).

Depending on the number of transported molecules and the direction of transport, carriers can be divided into uniporters, symporters and antiporters (exchangers) ([3] p. 239) (Figure 1). In symport and antiport, the movement of a solute down its electrochemical gradient is coupled to the migration of another solute against its electrochemical gradient. No such direct coupling can be observed in uniport ([3] p. 117) although it can be also driven by a primary active transport process ([3] p. 63).

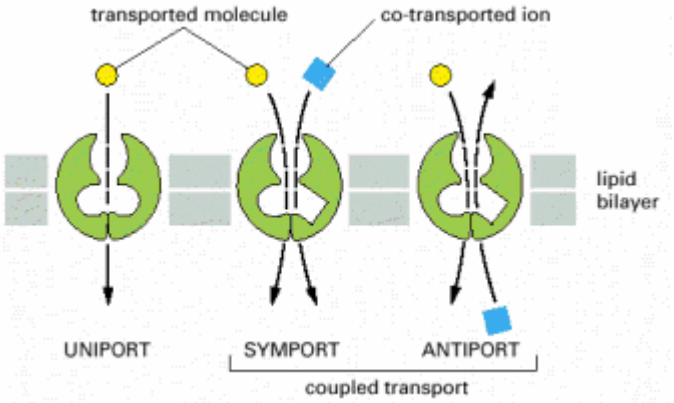

Figure 1 – Three types of carrier transport mechanisms [2] a) Uniporter transports one solute at a time in one direction. b) Symporter couples the transport of one or more molecules down their electrochemical gradient to the co-migration of other solutes against their electrochemical gradient. c) Antiporter couples the migration of one or more solutes down their electrochemical gradient to the counter-migration of other solutes against their electrochemical gradient.

1.1.2 Carrier transport kinetics

1.1.2.1 Kinetic models

The mechanism of carrier transport can be schematically represented by a carrier scheme. Depending on the structure and transport characteristics of the carrier, this scheme is more or less complicated. A simple scheme of a four-state carrier that transports one substrate is shown in Figure 2. An empty carrier oriented towards the inner side of the membrane (state E_i) can either undergo conformational changes and reorient itself to the outer side of the membrane (E_o) or form a carrier-substrate complex by binding a substrate (ES_i). This complex can be reoriented to the outer side of the membrane (ES_o) where substrate can be released (E_o) and consequently a new substrate bound (ES_o) and transported into the cell (ES_i). Each binding, releasing and reorientation reaction can be described by a rate constant as shown in Figure 2.

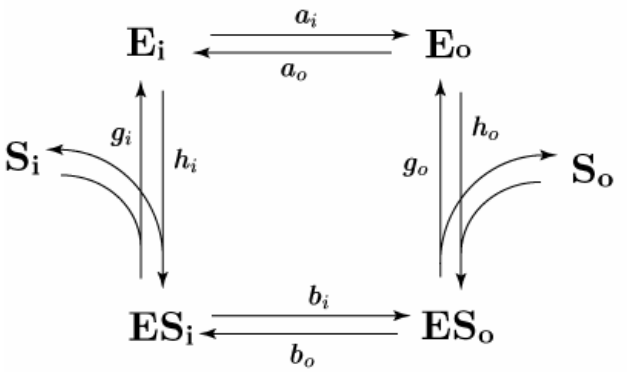

Figure 2 – Kinetic scheme of a general four-state carrier that can be used to describe a general uniporter. E_i is the state of an unbound carrier oriented inside the cell, E_o the state of an unbound carrier oriented towards the outside of the cell, ES_i is the state of a carrier-substrate complex oriented inside the cell, and ES_o stands for carrier-substrate complex oriented outside the cell. a_i and a_o are rate constants for reorientation of an empty carrier from inside to outside and outside to inside, respectively; b_i and b_o are rate constants for reorientation of a carrier-substrate complex from inside to outside and outside to inside, respectively; h_i and g_i are rate constants for binding and releasing of substrate inside the cell, respectively, and h_o and g_o are rate constants for binding and releasing of substrate outside the cell, respectively.

Symporters and antiporters are described by more complicated models involving six or even more steps depending on the transport mechanisms. General six-state symporter and antiporter models are shown in Figure 3. Symporters propagate solute gradients formed during primary active transport by transporting two or more different solutes together across the membrane. Antiporters, on the other hand, usually transport only one solute at a time as described by the so called ping-pong model. Antiport can be either obligatory (only exchange is possible because the empty carrier does not reorient itself – rate constants a_i and a_o in Figure 3 b) are both zero) or nonobligatory (carrier reorientation may occur even without exchange but at a slower rate – a_i and a_o have non-zero values but are smaller than b_i, b_o, f_i and f_o in Figure 3 b). ([3] p. 118 and p. 125). Both the obligatory and nonobligatory exchange exhibits trans-stimulation (transport stimulation by a solute on the other side of the membrane). In addition, we can distinguish between homoexchange (the same solute molecules are exchanged) and heteroexchange (molecules of different types are counter-transported) ([3] p. 118).

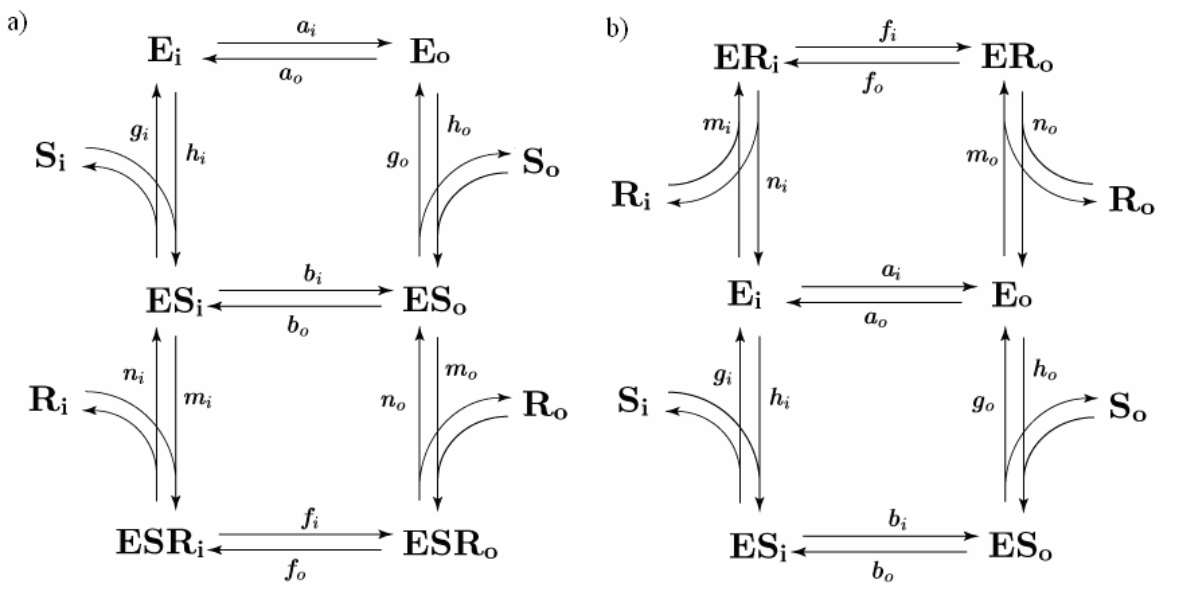

Figure 3 – Two examples of a six-state carrier model a) General scheme of a symporter co-transporting substrates S and R b) General scheme of an antiporter exchanging substrates S and R. Notation follows the same rules as in Figure 2.

Although this does not always reflect the real situation, a general carrier model is usually approximated with a model of a simple and symmetric carrier [7]. When a carrier is said to be symmetric, reorientation rate constants are the same for empty and loaded carrier (in the case of a four-state carrier, a_i equals b_i and a_o equals b_o in Figure 2). When a carrier is regarded as simple, substrate binding and releasing steps are considered to be much faster than reorientation steps (in a four-state carrier, rate constants g_i, h_i, g_o and h_o are considered to be much bigger than a_i, a_o, b_i and b_o in Figure 2) ([3] p. 118-119). Therefore, binding and releasing reactions can be fully described by a simple dissociation constant [7]. This traditional assumption of rapid substrate binding has been recently frequently questioned [8].

Alternatively, membrane transport can be described by a so called Multi-Substrate Single-File Model for Ion-Coupled Transporters. According to this theory, membrane transport is performed as hopping of substrates between the outer or inner solution and protein binding sites, and between binding sites within a single-file pore representing the transport protein. Rate constants are defined as hoping frequencies that describe the probability of individual hopping events. The Multi-Substrate Single-File Model includes local substrate-substrate interactions, but does not assume conformational changes of the transport protein. So far this theory can be applied only to unidirectional transport systems, and is able to reproduce some experimental data within experimental error. Its main advantage is the ability

to account for a broad spectrum of effects that occur in ion-coupled transporters (e.g. leakage currents, substrate flux coupling and variable stoichiometry) [9].

1.1.2.2 Kinetic equations

Unlike simple diffusion where transport rate is always proportional to substrate concentration, carrier mediated transport is substrate saturable because the supply of carriers in the membrane is limited. For one substrate to be transported by a carrier at a time, transport rate usually follows the Michaelis-Menten enzyme kinetics ([2], [3] p. 81 and p. 83):

$$v_o = \frac{v_{max} \cdot c^S{}_o}{K_m + c^S{}_o} \qquad (1)$$

where v_o is the initial transport rate, $c^S{}_o$ substrate concentration outside the cell, K_m the Michaelis-Menten constant and v_{max} the maximal velocity that is approached when substrate concentration is so high that the transport protein is almost permanently occupied.

When two or more molecules of the same type are co-transported in one transport cycle, transport kinetics changes to:

$$v_o = \frac{v_{max} \cdot (c^S{}_o)^n}{(K_{0,5\,m})^n + (c^S{}_o)^n} \qquad (2)$$

where n is the number of molecules transported together, and $K_{0.5m}$ is the substrate concentration at the half-maximum transport rate. In this case, the plot of transport rate versus substrate concentration is no longer hyperbolic as for the simple Michaelis-Menten kinetics but has a sigmoidal shape ([3] p. 85).

Kinetics schemes such as those presented in Figures 2 and 3 can also be described by Michaelis-Menten kinetic parameters with the expressions for v_{max} and K_m being a more or less complicated combination of rate constants depending on the complexity of the carrier model [8].

Carrier kinetics can be described by a system of linear differential equations. For the simplest case of a four-state carrier (Figure 2) and in the steady state, these equations have the form of:

$$\begin{vmatrix} -a_i - h_i \cdot c^S{}_i & a_o & g_i & 0 \\ a_i & -a_o - h_o \cdot c^S{}_o & 0 & g_o \\ h_i \cdot c^S{}_i & 0 & -b_i - g_i & b_o \\ 0 & h_o \cdot c^S{}_o & b_i & -b_i - g_o \end{vmatrix} \cdot \begin{vmatrix} NE_i \\ NE_o \\ NES_i \\ NES_o \end{vmatrix} = \begin{vmatrix} 0 \\ 0 \\ 0 \\ N^{tot} \end{vmatrix} \qquad (3)$$

In the non-steady state, a four-state carrier is described by the following system of equations:

$$\frac{d}{dt}\begin{vmatrix} NE_i \\ NE_o \\ NES_i \\ NES_o \end{vmatrix} = \begin{vmatrix} -a_i - h_i \cdot c^S{}_i & a_o & g_i & 0 \\ a_i & -a_o - h_o \cdot c^S{}_o & 0 & g_o \\ h_i \cdot c^S{}_i & 0 & -b_i - g_i & b_o \\ 0 & h_o \cdot c^S{}_o & b_i & -b_i - g_o \end{vmatrix} \cdot \begin{vmatrix} NE_i \\ NE_o \\ NES_i \\ NES_o \end{vmatrix} \qquad (4)$$

Rate constants have the same meaning as in Figure 2; NE_i is the occupancy of the carrier state E_i, NE_o occupancy of state E_o etc. N^{tot} stands for the total carrier state occupancy that is equal to the sum of NE_o, NE_i, NES_i and NES_o ([7] p. 386), and $c^S{}_i$ is the concentration of substrate S inside the cell. Equations 3 and 4 can be considerably simplified assuming that the carrier is simple and symmetric ([7] p. 363)

1.1.3 Effects of electrical fields on transport proteins

All membrane carriers operate within strong electrical fields (about 10^6 V·m^{-1}) that can dramatically affect transport. Firstly, voltage influences the energetics of carrier-mediated transport. Applied electric field affects the equilibrium between enzyme states because it changes their energy levels as well as energy barriers between them [10] as illustrated in Figure 4.

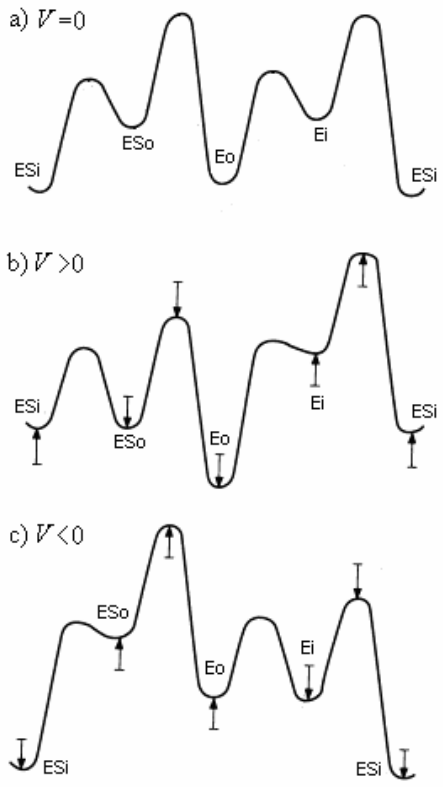

Figure 4 – Energy of the four-state carrier states vs. reaction coordinate for different membrane potential values: a) V=0 b) V>0 c)V<0 [10]

The effect of voltage on carrier transport energetics is independent of molecular mechanisms, and knowledge of the relevant electrochemical potentials and the overall stoichiometry is sufficient to calculate the equilibrium concentrations at a given voltage, the equilibrium voltage at given substrate concentrations, or the direction of net transport from the Nernst equation:

$$V^{eq} = \frac{R \cdot T}{z^S \cdot F} \cdot ln \frac{{c^S}_o{}^{eq}}{{c^S}_i{}^{eq}} \qquad (5)$$

where V^{eq} is the equilibrium potential (also called Nernst potential), R is the gas constant (R=8.314 $JK^{-1}mol^{-1}$), T is the thermodynamic temperature, z^S is the charge of the transported substrate, F is the Faraday constant (F=96485.34 $Cmol^{-1}$), and ${c^S}_i{}^{eq}$ and ${c^S}_o{}^{eq}$ refers to equilibrium substrate concentration inside and outside the cell, respectively ([3] p. 46).

Secondly and in contrast, voltage effects on the kinetics of carrier transport depend constitutively on the particular molecular mechanisms and are thus more complicated and richer in information. It was shown that changes in membrane potential could affect either the v_{max} of the transport or the K_m for the substrate or both v_{max} and K_m ([3] p. 227).

The basis for voltage effects on carrier kinetics are charge movements associated with individual reactions of the transport cycle. Specifically, both binding/releasing of substrates and conformational changes of the carrier may be associated with charge movements across the membrane electric field (termed “ion well effect” and “electroconformational coupling”, respectively). Ion well effect occurs because an ion moving from the aqueous solution to the protein binding site passes through a part of the transmembrane electric field, meaning that the equilibrium constants for ion binding become voltage dependent [6] (Figure 5). Electroconformational coupling can be described as a change of carrier properties in response to the actual membrane potential. It occurs because every molecule under an electric field tends to shift to a state with greater molar electric moment. This can be achieved for example by changing the charge of the carrier via dissociation of ionisable groups or reversible phosphorylation, by separation of charges, reorientation of permanent dipoles within the molecule, induction of dipoles by the electric field or by structural transition to a conformational state with higher macroscopic dipole moments[II]. As a result, a carrier oriented towards the inside of a cell may have a different arrangement of charges than a carrier oriented outside [10].

[II] Bernhard Schmitt, personal communication

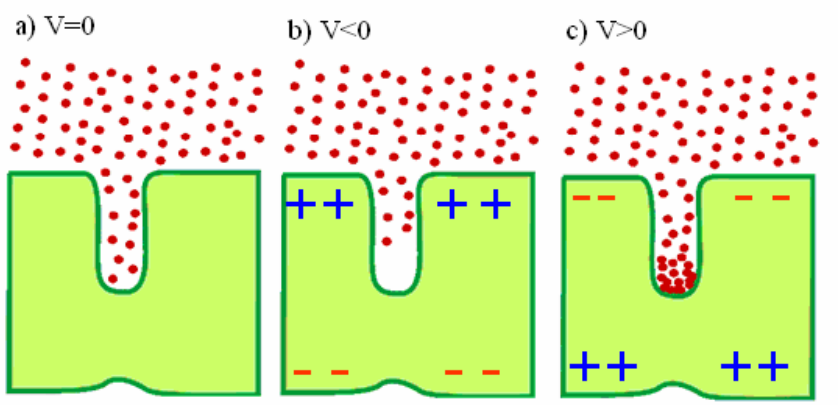

Figure 5 – Ion well effect for anion substrates a) Anions are evenly distributed around the carrier when membrane potential is zero. b) Ion depletion – in the case of a negative membrane potential, anions are repelled from the well by the negative charge inside the cell. c) Ion enrichment – when membrane potential is positive, anions are attracted by the well.

Since all the transport steps in carrier transport can be voltage dependent, the rate constants for these reactions have to be considered voltage dependent as well. The effect of voltage on individual reactions of the transport cycle representing the carrier model can be treated according to the theory of absolute reaction rates for narrow, symmetric energy barriers. The value of each reaction rate constant k_i^0 as observed in the absence of an electric field is therefore scaled by an exponential term into:

$$k_i = k_i^0 \cdot e^{\left(\frac{z^j \cdot u \cdot \delta_m}{2}\right)} \qquad (6)$$

Herein, z^j is the valence of the moving charge, u the non-dimensional voltage difference across the entire membrane, and δ_m the fraction of the total membrane potential that is traversed by the moving charge in the outward direction; inward movement reverses the sign of the exponent. Thus, total voltage partitions into fractions δ_1 to δ_3 traversed by the substrate during binding or releasing inside the cell (δ_1), during carrier reorientation (δ_2), and during binding or releasing outside the cell (δ_3), respectively (Figure 6). These membrane potential fractions fulfil the equation:

$$\delta_1 + \delta_2 + \delta_3 = 1 \qquad (7)$$

During reorientation of an empty or loaded carrier, multiple individual charges ζ_{2k} of different physical nature (e.g. ionic charges on the carrier, dipoles or induced dipoles) may move over fractions δ_{2k} that are not necessarily the same as the fraction δ_2 valid for the ionic

substrate. For simplicity, all charge movements during a given reorientation step can be lumped together into a single equivalent charge z^j such that:

$$\sum_{i=1}^{n} \zeta_i \cdot \delta_k = z^j \cdot \delta_2 \qquad (8)$$

[6,11]. Similarly, the Multi-Substrate Single-File Model for Ion-Coupled Transporters also supposes rate constants (hopping rates for charged substrates) to be voltage dependent [9].

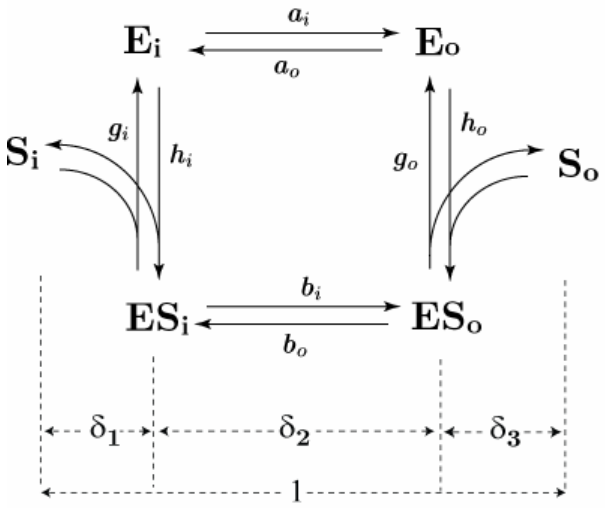

Figure 6 – Four-state carrier scheme with membrane potential fractions δ_1, δ_2 and δ_3 shown. δ_1 is the part of membrane potential sensed by substrate binding or releasing reactions inside the cell, δ_2 is sensed by carrier reorientation steps, and δ_3 by substrate binding or releasing outside the cell.

Depending on the charge of transported molecules, carriers can be either electrogenic (move electric charge across the membrane) or electroneutral [5] (Figure 7). Importantly, ion well effect and electroconformational coupling mechanisms also apply fully to electroneutral transport [12]. Although Nernst Equation 5 does not apply to electroneutral uniporters, their reorientation is still influenced by voltage due to carrier charge effects. Moreover, ion well effect comes into play when two oppositely charged substrates are co-transported or two substrates of the same charge exchanged by an electroneutral six-state carrier.

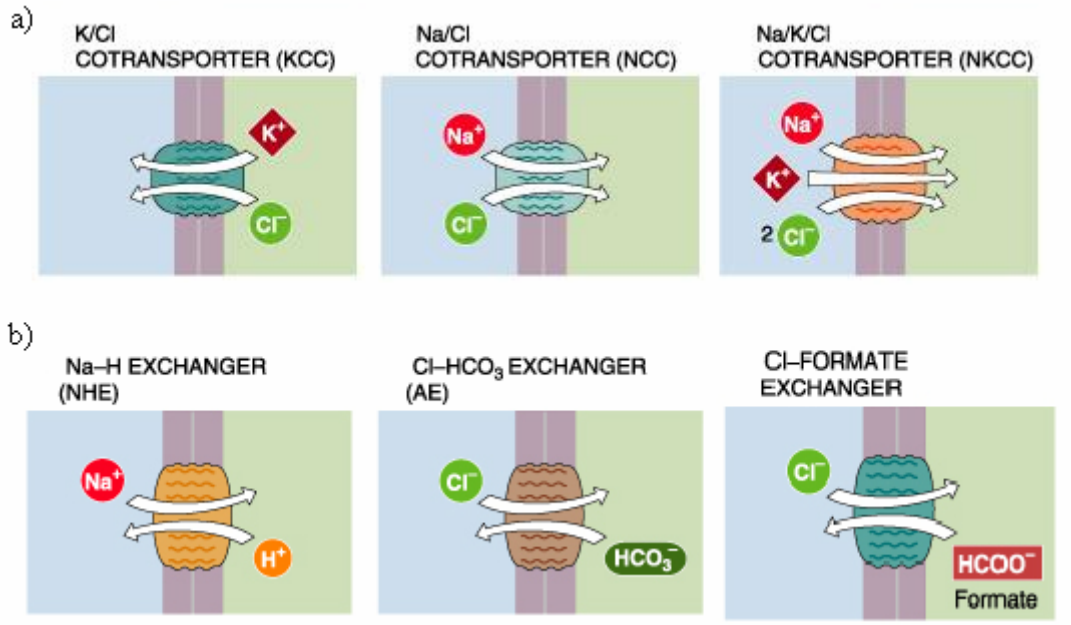

Figure 7 – Examples of electroneutral transporters: a) electroneutral symporters b) electroneutral antiporters [13]

1.1.3.1 Constant membrane potential

Membrane potential (voltage difference between two sides of the plasma membrane) arises due to the presence of large concentration gradients for ions across the membrane. These gradients are caused by the activity of ion channels, carriers and pumps [14,15]. Usually, membrane potential is formed either by pumping of protons (in mitochondria, chloroplasts, yeasts and bacteria) or by the concentration gradient of Na^+ (in animal cells and some bacterial cells). Negative membrane potential is unconditionally required for bacterial cells to produce ATP from ADP while in animal cells (where ATP is produced in mitochondria) membrane potential stabilises the cell osmotically [16]. In non-excitable cells, membrane potential has a relatively stable resting potential value (usually between -40 mV to -90 mV depending on the cell type) [5]. However, membrane potential depolarisation or hyperpolarisation can be caused by influxes or effluxes of cations such as Na^+, Ca^{2+}, and K^+ [5,15]. Carrier proteins are influenced by the actual value of membrane potential, and because it is not necessarily static, also by its frequency and amplitude.

1.1.3.2 Oscillating electric field

Oscillating electric fields have been widely observed around cells [17]. They can be caused for example by the opening and closing of ion channels, by the activity of membrane pumps (it has been shown that Na^+,K^+-ATPase can give rise to oscillating electric fields, for example), by the presence of action potential cells such as cardiac cells, by an oscillating substrate concentration or by an externally applied electric field that is greatly magnified in

the membrane [18-20]. The question how oscillating electric fields influence transport via membrane proteins is central to neurophysiology [18]. It has been shown experimentally that ion net movement via Na^+,K^+-ATPase depends on the frequency and amplitude of the applied oscillating electric field [21]. Using small amplitude approximation, the average flux in the presence of a periodic potential can be theoretically described as a sum of Lorentzian functions [12]. Many transport proteins are able to transduce free energy from a periodic electric field (such as a sinusoidal or square wave field) to chemical or transport work [11,21]. Net cyclic flux can also be induced by randomly oscillating electric fields (electric noise) [22]. For example, electric fields which fluctuate both in life time and amplitude can induce ion pumping by Na^+,K^+-ATPase [23]. However, electric noise resulting from the environment around a carrier cannot be transduced to work as it is not completely random but correlated to the state that the enzyme is in [22].

1.2 MntH transport protein

The goal of our work was to study some of the transport properties of the MntH protein, a metal ion transporter playing an important role in bacterial homeostasis and virulence. MntH belongs to a highly conserved Nramp protein family, whose members can be found in all different kinds of organisms including mammals, plants and yeast. Therefore, this chapter presents a brief summary of the main characteristics of transporters belonging to this family with an emphasis on their transport mechanisms.

1.2.1 Metal ions

Metal ions are important for all cells and their homeostasis is crucial for life. Transition metals such as Fe^{2+}, Mn^{2+}, Zn^{2+} and Co^{2+} are essential for many biological processes – they are involved in cell metabolism (as cofactors of many enzymes), gene regulation, free-radical homeostasis and signal transduction pathways [24]. Toxic metals like Cd^{2+} and Ni^{2+} interfere in various ways with homeostasis or function of the essential metals [25]. An adequate supply of metal ions is vital, but these essential nutrients are toxic at elevated levels. Therefore, shortage or excess in metal ion might cause death or severe illness such as haemochromatosis, neurodegenerative diseases (e.g. Parkinson's and Alzheimer's disease), Wilson's and Menkes disease (all caused by metal ion overload in man) or anaemia (a consequence of metal ion deficiency in man). Therefore, ion transporters maintain the correct concentration of metal ions in every cell through a highly regulated process of metal uptake, storage and secretion [25,26]. A high level of regulation is crucial because limited

activity of a single metal ion transporter may inhibit cell growth due to the shortage of a vital metabolic element, and excess transporter activity may be toxic and lead to cell death [24].

Acquisition of iron and manganese, which we are going to discuss later on, is vital because both metals contribute to energy metabolism, electron and oxygen transport, DNA synthesis, cell protection against oxidative stress, and are important for virulence [27]. The cellular requirements for manganese (submicromolar levels) are generally much lower than for iron [28]. However, Mn^{2+} is necessary to both free-living and pathogenic bacterial cells for nutrient and defence purposes [27,29]. Most of the known bacterial Mn^{2+}-containing enzymes function either in stress response or in energy metabolism (for example in the metabolism of nitrogen and oxygen, including toxic radicals) [27,29,30]. They are key players in signal transduction pathways, impart increased resistance to early killing by macrophages, and are necessary during interaction with an eukaryotic host and for the survival in stationary phase [31,32]. Mn^{2+} contributes to resistance against reactive oxygen species (peroxides and superoxides) both enzymatically and independent of any enzyme ([32] and references therein). Finally, Mn^{2+} can function in place of Mg^{2+} in a variety of both structural and catalytic roles [32].

1.2.2 Nramp family of transport proteins

Members of the family of Natural resistance-associated macrophage proteins (Nramp) are secondary metal ion transporters that play a major role in metal ion homeostasis in a large spectrum of organisms including mammals, plants, yeast, and bacteria ([25,33] and references therein). Members of this family can transport divalent metal cations such as Mn^{2+}, Zn^{2+}, Cu^{2+}, Fe^{2+}, Cd^{2+}, Ni^{2+} and Co^{2+} using energy stored in H^+ electrochemical gradients [34-36]. The Nramp family is represented by three members in yeast (SMF1, SMF2, and SMF3), in fly by MVL (*malvolio*) and in mammals by Nramp1 (also called SLC11 A1 – solute carrier family 11) and Nramp2 (also called DCT1 – divalent cation transporter 1, DMT1 – divalent metal transporter 1, and SLC11 A2) [33]. Bacterial Nramp-like transporters were named MntH (Manganese transporters H^+-dependent) proteins [36].

The Nramp protein family is extremely conserved through evolution [37]. It consists of 5 phylogenetic groups – 3 bacterial groups (MntH A, MntH B and MntH C) and 2 eukaryotic groups (prototypical and archetypical group). The existence of bacterial Nramp homologs suggests that the Nramp family originated in prokaryotes [38,39]. Members of the Nramp family possess a common topological organisation that is defined by the presence of a highly

conserved hydrophobic core encoding 10 transmembrane (TM) segments (that include several invariant charged residues) and either one or two non-conserved, highly hydrophobic TM domains. Eukaryotic Nramps have 12 TM domains and both the N- and C-termini are cytoplasmic (with an exception of yeasts that have 11 TM segments). Bacterial Nramps consist of 11 TM domains, their N-terminus is cytoplasmic and the C-terminus is in the periplasm [33,40].

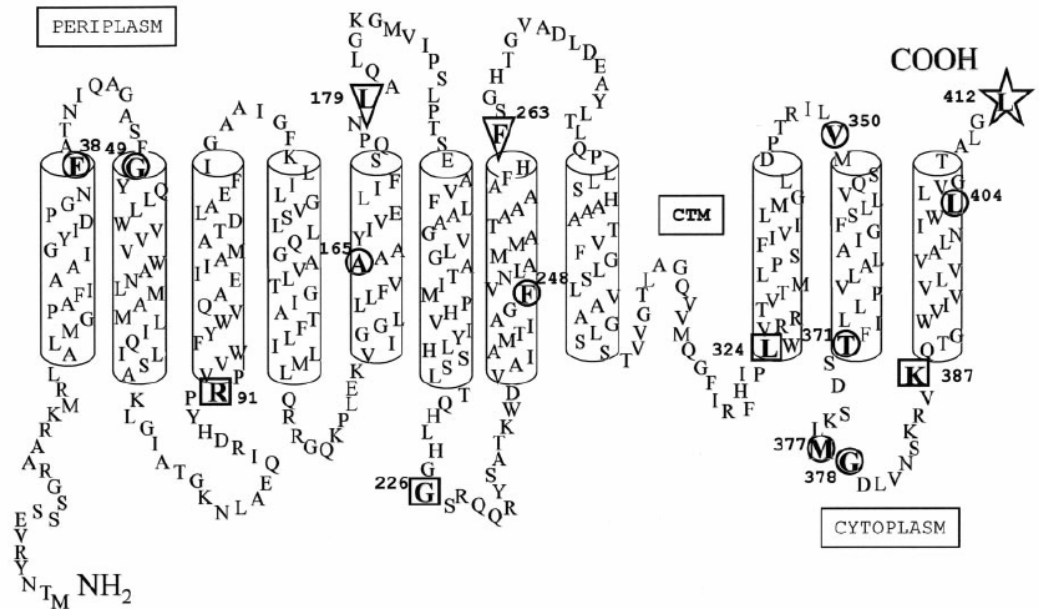

Figure 8 – Predicted topology of the bacterial MntH protein. MntH C-terminus is periplasmic together with the loops between TM segments 1/2, 3/4, 5/6, 7/8, and 9/10, the N-terminus is cytoplasmic and followed by 11 transmembrane segments [40].

1.2.2.1 Yeast SMF1, SMF2 and SMF3 transporters

SMF proteins catalyze proton-dependent uptake of divalent cations in yeast [34,41,42]. Smf1p is located in the yeast plasma membrane, facilitates cell-surface uptake of Mn^{2+} into the cytoplasm and helps to resist chelator stress. Smf2p mediates Mn^{2+} efflux from endocytic vehicles [43], and Smf3p is found in the membrane of yeast vacuoles [44].

Besides Mn^{2+}, Smf1p is also able to transport Fe^{2+} and Co^{2+} but at a much lower rate. Zn^{2+} was found to be an inhibitor of Mn^{2+} transport by Smf1p; it binds to the same site as Mn^{2+} and enables protons to slip through the transporter but is not transported [42]. Fe^{2+} and Mn^{2+} uptake is inhibited by Na^{+} in a *pH*-dependent way. Inhibition increases with *pH* elevation and is not dependent on metal ion concentration. This suggests that sodium competes with protons for the same binding site and slips across the transporter in the proton

pathway [42,45]. This Na^+ slip acts probably as a protection against toxic metal ion accumulation under conditions of increasing salt concentration [34,42].

1.2.2.2 Mammalian Nramp1 transporters

Nramp1 functions almost exclusively in metal (such as Fe^{2+}, Mn^{2+} and Co^{2+}) transport across the phagosomal membrane of macrophages and is therefore necessary for the defence against bacterial infection [46,47]. It is expressed in the lysosomal compartment of macrophages and neutrophils and recruited to the membrane of the pathogen-containing phagosomes upon phagocytosis [48-50]. The expression of *NRAMP1* is strictly regulated and stimulated by inflammatory signals [47]. Upon a bacterial infection, the invading bacterium is taken into the macrophage phagosome where it is challenged by reactive oxygen components. The infecting pathogen protects itself by producing metalloenzymes that can neutralize the toxic agents. The macrophage defence is based on the deprivation of the engulfed bacterium of the required metal ions (Fe^{2+} and Mn^{2+}) by the activity of Nramp1 that co-transports metal-ions and protons from the phagosomal lumen into the cytoplasm. This restricts the ability of the pathogen to produce and activate protective enzymes, and avoids the propagation of the ingested microorganisms [24,41]. Defective Nramp1 causes sensitivity to several bacterial and protozoal intracellular pathogens (including *Salmonella typhimurium, Mycobacterium tuberculosis*, *Mycobacterium leprae*, *Mycobacterium avium* and *Leishmania donovani*) by impairing the ability of macrophages to control intracellular microbial replication ([32] and references therein).

1.2.2.3 Mammalian Nramp2 (DCT1, DMT1, SLC11) transporters

Nramp2 is the major non-transferrin-dependent iron uptake system in mammals that functions as a proton co-transporter with an unusually broad substrate specificity including Mn^{2+}, Zn^{2+}, Co^{2+}, Cd^{2+}, Cu^{2+}, Ni^{2+} and Pb^{2+}. Both human and mouse Nramp2 proteins are expressed in most cell types and in many different tissues (e.g. intestine, brain and kidney) [35]. Genetic studies in rat and mouse models revealed that Nramp2 is unconditionally required for the maintenance of life. Mutations in Nramp2 affect iron homeostasis, and cause defects in intestinal iron uptake resulting in severe iron disorders (mycrocytic anaemia and serum and hepatic overload) [26]. Nramp2 deficient rats also show marked Mn^{2+} deficiency [51].

Nramp2 mediated metal ion transport is H^+-coupled, driven by the H^+ electrochemical potential gradient, and voltage dependent. The stoichiometry between H^+ and the divalent

metal ion ligands transported by Nramp2 varies in different conditions (e.g. *pH* and voltage). At neutral *pH*, approximately one proton is translocated per divalent metal ion transported. This mechanism is supposed to have a physiological significance because it ensures a constant uptake of divalent metal ions [35]. However, increasing the driving force by lowering the *pH* or imposing a highly negative potential generates a proton slip that is dependent on the presence of metal ions in the medium and influenced by the membrane potential (ratio H^+/Me^{2+} increases as membrane potential becomes more negative inside) [34,52]. This "proton slippage" probably has a physiological advantage and was positively selected during evolution as a protection against metal intoxication by overloading [25,42]. In addition, co-transported H^+ can result in a slight lowering of *pH* at the intracellular surface of the membrane, sufficient to maintain the solubilisation of iron before its binding to intracellular proteins [35]. Moreover, because H^+ binding and translocation may proceed at low outer *pH* even in the complete absence of metal ions, Nramp2 can operate as an H^+ uniporter [1,35].

The third mode of function of Nramp2 was described by [1], where Fe^{2+} transport that is not associated with H^+ influx (and is therefore driven only by the electrochemical gradient for Fe^{2+}) was observed at mildly basic *pH* values. Because a six-state carrier model cannot sufficiently explain the presence of an uncoupled metal ion leak, an eight-state Nramp2 model was proposed in [1] to describe these effects. The most general eight-state kinetic scheme would have the form of a cube [6], but because Fe^{2+} concentration was experimentally shown to be the limiting factor of the Fe^{2+} and H^+ co-transport rate suggesting that binding of protons precedes Fe^{2+} binding, the eight-state cubic scheme can be reduced to the form shown in Figure 9 [1].

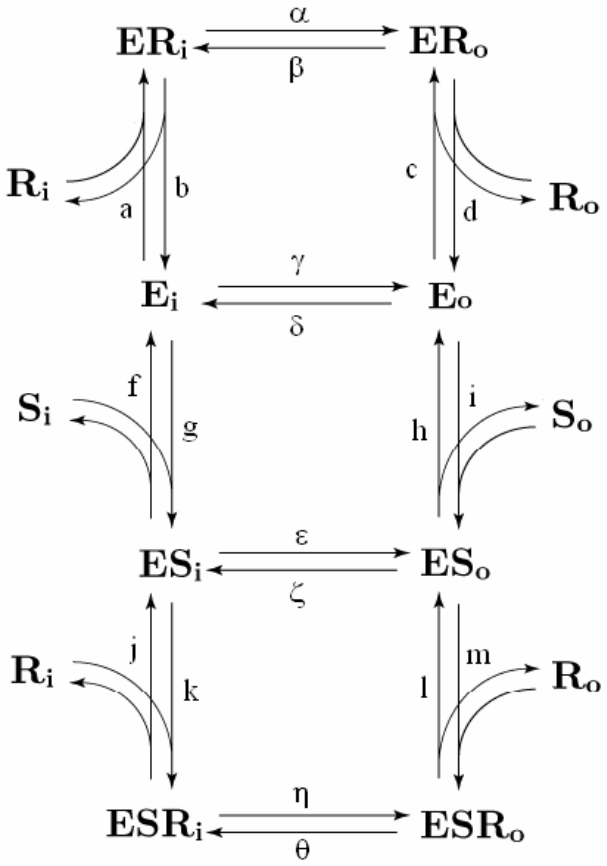

Figure 9 – Eight-state carrier model introduced in [1] to describe the transport mechanism of Nramp2 (for Nramp2, substrate S represents protons and substrate R metal ions, e.g. Fe^{2+})

1.2.2.4 Bacterial MntH transporters

Because Nramp proteins probably originated in prokaryotes, bacterial MntH transporters are attractive prototypic models that can be used to study the mechanism of transport in this conserved family [40]. MntH proteins function as proton-dependent secondary divalent metal ion transporters with a broad range of metal substrates similar to Nramp2 [32,36,53]. Fe^{2+} transport mediated by MntH does not appear to be physiologically relevant for the bacterium since free Fe^{2+} concentration unlikely to occur in biological systems would be required for significant rates of uptake. MntH is the main transporter ensuring Mn^{2+} influx in *Escherichia coli* and *Salmonella Typhimurium* [32]. However, disruption of *mntH* did not affect bacterial growth under aerobic conditions in either minimal or rich medium, implying that MntH is not essential for growth in normal laboratory conditions [36]. This suggests that other bacterial Mn^{2+} transporters including ABC-type and P-type ATPases can compensate for the loss of MntH-mediated Mn^{2+} uptake ([32] and references therein).

Similarly to mammalian Nramp1 proteins that are involved in resistance to microbial pathogens, bacterial MntH transporters are also involved in pathogenesis. When invading a mammalian host, a major task for the bacteria is to manipulate the local environment so as to ensure protection against the immunity response of the infected host [32]. One of the bacterial responses upon entering an Nramp1-expressing macrophage is the induction of MntH and rapid accumulation of available Mn^{2+} [32,54]. Increased intracellular Mn^{2+} concentration is then utilized by the bacterium in the response to reactive oxygen and nitrogen species being encountered. In this way, competition for Mn^{2+} between MntH and mammalian Nramp1 occurs [32]. In both *E. coli* and *S. Typhimurium*, transport of Mn^{2+} by MntH proteins was shown to be important for full virulence [32,54]. *MNTH* transcription is independently regulated by the presence of reactive oxygen species (especially H_2O_2) and Mn^{2+} and Fe^{2+} [29,32,55]. The possibility of MntH regulation by Fe^{2+} might be explained by the fact that either the $[Mn^{2+}]/[Fe^{2+}]$ ratio or the total content of these two divalent metals is under strict homeostatic control [29].

2 Experimental methods

2.1 Measurements of membrane potential and intracellular *pH* in *E. coli*

In our experiments, bacterial strains derived from the *E. coli* DH11S *mntH* strain (with a deleted gene for MntH) [40] were used. This strain itself is resistant to kanamycine, and spectinomycine resistance was induced in some of the strains due to the transformation by plasmid pGBM6-pHL that carries the gene for pHluorin, a *pH*-sensitive Green Fluorescent Protein (GFP). pBAD plasmid carried ampicillin resistance, and in some of the strains also the gene for MntH. While *pHLUORIN* expression was constitutive, *MNTH* expression needed to be induced by L-arabinose. Detailed characteristics of six *E. coli* strains that were used in our experiments are shown in Table 1.

Strain	ATB resistance	pHluorin	Mutation	Note
pBAD+pHl	A, K, S	yes		Negative control
EcoliA+pHl	A, K, S	yes		Contains MntH
pBAD	A, K	no		Negative control
EcoliA	A, K	no		Contains MntH
N401G	A, K, S	yes	Asparagine 401 to glycine	Contains MntH
D34G	A, K, S	yes	Aspartic acid 34 to glycine	Contains MntH

Table 1 – *E. coli* strains used in our experiments. A – ampicilline, K – kanamycine, S – spectinomycine

Bacterial cells were cultivated in Luria-Bertani medium (LB medium) that contains 1% Bacto-trypton, 0.5% Bacto-yeast extract, 0.5% NaCl and appropriate antibiotics (0.015% kanamycine, 0.05% ampicilline and 0.05% spectinomycine when required). In addition, 1.5% Bacto-agar was added to solid agar medium. Using a wire loop, we inoculated a single bacterial colony from the agar plate into 2 ml of LB medium. Cells were grown overnight at 37 $^{\circ}$C and 250 rpm, diluted hundred times in the morning and incubated for two hours. Next, 0.06% L-arabinose was added and cells were incubated for another hour. K_2HPO_4 buffers, whose *pH* was adjusted to desired values (4.7 and 5.5) using citric acid, were used to wash the cells twice and dilute them to the desired optical density 0.2 (measured at 600 nm by a digital spectrometer Novaspec III).

Redistribution fluorescent dye diS-C_3(3) (3,3'-dipropylthiocarbocyanine iodide) was used to monitor the membrane potential in *E. coli* cells. Compared to another carbocyanine dye, diS-C_3(5) (3,3'-dipropylthiodicarbocyanine iodide), which contains a pentamethine bridge, diS-C_3(3) has a trimethine bridge and therefore lacks the tendency to form non-fluorescent aggregates at high dye concentrations [56,57]. Its response to the membrane potential is more complex and enables ratiometric measurements [58], whereas diS-C_3(5) just changes its fluorescence intensity upon membrane potential shifts.

diS-C_3(3), as a membrane permeant cation, is redistributed according to the Nernst Equation 5 between the extracellular medium and the intracellular space, where it binds to cellular macromolecules such as lipids, proteins and nucleic acids. This binding immediately alters its spectroscopic signal by shifting the fluorescence spectrum of the bound dye towards longer wavelengths and by increasing its fluorescence intensity [56,59]. As a response to

membrane potential shifts, diS-C_3(3) changes its intracellular concentration. This can be measured as a shift in the fluorescence maximum wavelength position (blue shift is caused by depolarisation and consequent dye efflux, and red shift occurs due to hyperpolarisation that causes dye uptake) [59] or ratiometrically, as a ratio at two selected emission wavelengths [58].

Spectroscopic measurements were performed on a spectrofluorimeter Fluoromax-2 (Jobin-Yvon SPEX). We measured either the whole diS-C_3(3) emission spectra at an excitation wavelength 531 nm, or only the ratio of the emission intensity at 580 nm and 560 nm [58]. Thus, the red shift of the emission spectra was reflected by higher values of the selected ratio. Before diS-C_3(3) and metal ions were added, signal from the cell suspension was determined; this value was then subtracted from emission intensities measured after the addition of the dye or metal ions.

In *pHLUORIN* expressing strains N401G and D34G, the possibility of simultaneous membrane potential measurements (using the diS-C_3(3) dye) and intracellular *pH* (pH_i) measurements (using pHluorin) was explored. Therefore, in addition to diS-C_3(3) emission intensity ratio measurements, pHluorin emission intensity ratios for two different excitation wavelengths (410 nm and 470 nm) at an emission wavelength 520 nm were measured.

2.2 Mathematical modelling

For the purpose of our modelling, we supposed that substrates form an infinite reservoir on both sides of the membrane ensuring that substrate concentration does not change with time. This means that our models simulate the initial transport phase where substrate fluxes are too small to affect the overall substrate concentration inside or outside the cell. Applied voltage was assumed to be infinitely effectively regulated to maintain a constant value in the case of a constant membrane potential or to have a desired time course in the case of oscillating membrane potential (as would be the case in a voltage-clamp experiment). Our models were simulated for a sufficiently long time to enable the system to reach the stationary state.

We found the kinetic equations for a general four-state carrier in ([7] p. 387), and built up equations for general six-state and eight-state carriers. We modified the standard carrier kinetic models by incorporating the voltage dependence of all rate constants according to the Eyring theory of absolute reaction rates [6,60] (see Equation 6).

Thus, the rate constants describing a four-state carrier have the form of:

$$\begin{aligned} a_i &= a_i^0 \cdot e^{\left(\frac{z^C \cdot u \cdot \delta_2}{2}\right)} & a_o &= a_o^0 \cdot e^{\left(\frac{-z^C \cdot u \cdot \delta_2}{2}\right)} \\ b_i &= b_i^0 \cdot e^{\left(\frac{\left(z^C + z^S\right) \cdot u \cdot \delta_2}{2}\right)} & b_o &= b_o^0 \cdot e^{\left(\frac{-\left(z^C + z^S\right) \cdot u \cdot \delta_2}{2}\right)} \\ g_i &= g_i^0 \cdot e^{\left(\frac{-z^S \cdot u \cdot \delta_1}{2}\right)} & g_o &= g_o^0 \cdot e^{\left(\frac{z^S \cdot u \cdot \delta_3}{2}\right)} \\ h_i &= h_i^0 \cdot e^{\left(\frac{z^S \cdot u \cdot \delta_1}{2}\right)} & h_o &= h_o^0 \cdot e^{\left(\frac{-z^S \cdot u \cdot \delta_3}{2}\right)} \end{aligned} \qquad (10)$$

where x_y^0 refers to initial rate constant values valid before voltage is switched on, z^C is the charge of the carrier and z^S charge of substrate S. These equations were incorporated into the non-steady state Equation 4 presented in ([7] p. 387) to describe a four-state carrier.

Substrate influx ΔS_i through a four-state uniporter was calculated as the amount of substrate released inside the cell minus the amount of substrate bound to the carrier oriented towards the inside of the cell:

$$\Delta S_i = g_i \cdot NES_i - h_i \cdot c^S{}_i \cdot NE_i \qquad (11)$$

Analogically, substrate efflux ΔS_o can be expressed as:

$$\Delta S_o = g_o \cdot NES_o - h_o \cdot c^S{}_o \cdot NE_o \qquad (12)$$

For a four-state carrier, the principle of detailed balance saying that in equilibrium, the overall rate for traversing a reaction cycle clockwise equals the rate for traversing it anticlockwise ([7] p. 389) leads to equation:

$$a_i \cdot h_o \cdot c^S{}_o^{eq} \cdot b_o \cdot g_i = a_o \cdot h_i \cdot c^S{}_i^{eq} \cdot b_i \cdot g_o \qquad (13)$$

where $c^S{}_i^{eq}$ and $c^S{}_o^{eq}$ refers to equilibrium substrate concentration inside and outside the cell, respectively. In equilibrium (when no substrate flux occurs), inside and outside substrate concentrations fulfil Nernst Equation 5. For a given applied membrane potential V^{eq}, Equation 13 can be therefore written in the form of:

$$e^{\left(\frac{V^{eq} \cdot F \cdot z^S}{R \cdot T}\right)} = \frac{a_o \cdot h_i \cdot b_i \cdot g_o}{a_i \cdot h_o \cdot b_o \cdot g_i} \qquad (14)$$

To obey the principle of detailed balance in our simulations, Equation 14 was used to calculate the rate constant a_i.

For an electroneutral uniporter (z^S=0), Equation 14 is reduced to:

$$a_i \cdot h_o \cdot b_o \cdot g_i = a_o \cdot h_i \cdot b_i \cdot g_o \qquad (15)$$

In the case of an electrogenic four-state carrier, Equations 10 describing the voltage dependence of rate constants defines how the exponential term in Equation 14 is divided into various voltage steps. Moreover, when z^C is different from zero, Equation 10 incorporates the effect of carrier charge on carrier reorientation.

Non-steady state kinetic equations describing a six-state symporter co-transporting substrates S and R (Figure 3 a)) were created in the form of:

$$\frac{d}{dt}\begin{vmatrix} NE_i \\ NE_o \\ NES_i \\ NES_o \\ NESR_i \\ NESR_o \end{vmatrix} = A \cdot \begin{vmatrix} NE_i \\ NE_o \\ NES_i \\ NES_o \\ NESR_i \\ NESR_o \end{vmatrix}$$

$$A = \begin{vmatrix} -a_i - h_i \cdot c^S{}_i & a_o & g_i & 0 & 0 & 0 \\ a_i & -a_o - h_o \cdot c^S{}_o & 0 & g_o & 0 & 0 \\ h_i \cdot c^S{}_i & 0 & -b_i - m_i \cdot c^R{}_i - g_i & b_o & n_i & 0 \\ 0 & h_o \cdot c^S{}_o & b_i & -b_o - g_o - m_o \cdot c^R{}_o & 0 & n_o \\ 0 & 0 & m_i \cdot c^R{}_i & 0 & -n_i - f_i & f_o \\ 0 & 0 & 0 & m_o \cdot c^R{}_o & f_i & -f_o - n_o \end{vmatrix} \qquad (16)$$

Rate constants in Equation 16 depend on applied voltage as follows:

$$a_i = a_i{}^0 \cdot e^{\left(\frac{z^C \cdot u \cdot \delta_2}{2}\right)} \qquad a_o = a_o{}^0 \cdot e^{\left(\frac{-z^C \cdot u \cdot \delta_2}{2}\right)}$$

$$b_i = b_i{}^0 \cdot e^{\left(\frac{\left(z^C + z^S\right) \cdot u \cdot \delta_2}{2}\right)} \qquad b_o = b_o{}^0 \cdot e^{\left(\frac{-\left(z^C + z^S\right) \cdot u \cdot \delta_2}{2}\right)}$$

$$f_i = f_i{}^0 \cdot e^{\left(\frac{\left(z^C + z^S + z^R\right) \cdot u \cdot \delta_2}{2}\right)} \qquad f_o = f_o{}^0 \cdot e^{\left(\frac{-\left(z^C + z^S + z^R\right) \cdot u \cdot \delta_2}{2}\right)}$$

$$g_i = g_i{}^0 \cdot e^{\left(\frac{-z^S \cdot u \cdot \delta_1}{2}\right)} \qquad g_o = g_o{}^0 \cdot e^{\left(\frac{z^S \cdot u \cdot \delta_3}{2}\right)} \qquad (17)$$

$$h_i = h_i{}^0 \cdot e^{\left(\frac{z^S \cdot u \cdot \delta_1}{2}\right)} \qquad h_o = h_o{}^0 \cdot e^{\left(\frac{-z^S \cdot u \cdot \delta_3}{2}\right)}$$

$$m_i = m_i{}^0 \cdot e^{\left(\frac{z^R \cdot u \cdot \delta_1}{2}\right)} \qquad m_o = m_o{}^0 \cdot e^{\left(\frac{-z^R \cdot u \cdot \delta_3}{2}\right)}$$

$$n_i = n_i{}^0 \cdot e^{\left(\frac{-z^R \cdot u \cdot \delta_1}{2}\right)} \qquad n_o = n_o{}^0 \cdot e^{\left(\frac{z^R \cdot u \cdot \delta_3}{2}\right)}$$

Nernst equation together with the principle of detailed balance leads to the following condition for rate constants describing a six-state symporter:

$$e^{\left(\frac{F\cdot\left(V_S^{eq}\cdot z^S + V_R^{eq}\cdot z^R\right)}{R\cdot T}\right)} = \frac{a_o\cdot h_i\cdot m_i\cdot f_i\cdot n_o\cdot g_o}{a_i\cdot h_o\cdot m_o\cdot f_o\cdot n_i\cdot g_i} \qquad (18)$$

where V_S^{eq} and V_R^{eq} are the equilibrium membrane potentials for the S and R substrate, respectively, and z^R is the charge of the co-transported substrate R. In our simulations, rate constant a_i was calculated from Equation 18 to ensure that the principle of detailed balance is observed. For a six-state carrier, influxes of substrates S (ΔS_i) and R (ΔR_i) were calculated as follows:

$$\Delta S_i = g_i\cdot NES_i - h_i\cdot c^S{}_i\cdot NE_i \qquad (19)$$

$$\Delta R_i = n_i\cdot NESR_i - m_i\cdot c^R{}_i\cdot NES_i \qquad (20)$$

Non-steady state differential equations describing the eight-state carrier model introduced in [1] (Figure 9) have the form of:

$$\frac{d}{dt}\begin{vmatrix} NE_i \\ NE_o \\ NES_i \\ NES_o \\ NER_i \\ NER_o \\ NESR_i \\ NESR_o \end{vmatrix} = B\cdot \begin{vmatrix} NE_i \\ NE_o \\ NES_i \\ NES_o \\ NER_i \\ NER_o \\ NESR_i \\ NESR_o \end{vmatrix} \qquad (21)$$

$$B = \begin{vmatrix} -a\cdot c^R{}_i - \gamma - g\cdot c^S{}_i & \delta & f & 0 & b & 0 & 0 & 0 \\ \gamma & -c\cdot c^R{}_o - \delta - i\cdot c^S{}_o & 0 & h & 0 & d & 0 & 0 \\ g\cdot c^S{}_i & 0 & -f-\varepsilon-k\cdot c^R{}_i & \zeta & 0 & 0 & j & 0 \\ 0 & i\cdot c^S{}_o & \varepsilon & -h-\zeta-m\cdot c^R{}_o & 0 & 0 & 0 & l \\ a\cdot c^R{}_i & 0 & 0 & 0 & -\alpha-b & \beta & 0 & 0 \\ 0 & c\cdot c^R{}_o & 0 & 0 & \alpha & -\beta-d & 0 & 0 \\ 0 & 0 & k\cdot c^R{}_i & 0 & 0 & 0 & -j-\eta & \theta \\ 0 & 0 & 0 & m\cdot c^R{}_o & 0 & 0 & \eta & -l-\theta \end{vmatrix}$$

In Equation 21, rate constants are voltage dependent according to the following equations:

$$
\begin{aligned}
a &= a^0 \cdot e^{\left(\frac{z^R \cdot u \cdot \delta_1}{2}\right)} & b &= b^0 \cdot e^{\left(\frac{-z^R \cdot u \cdot \delta_1}{2}\right)} \\
c &= c^0 \cdot e^{\left(\frac{-z^R \cdot u \cdot \delta_3}{2}\right)} & d &= d^0 \cdot e^{\left(\frac{z^R \cdot u \cdot \delta_3}{2}\right)} \\
f &= f^0 \cdot e^{\left(\frac{-z^S \cdot u \cdot \delta_1}{2}\right)} & g &= g^0 \cdot e^{\left(\frac{z^S \cdot u \cdot \delta_1}{2}\right)} \\
h &= h^0 \cdot e^{\left(\frac{z^S \cdot u \cdot \delta_3}{2}\right)} & i &= i^0 \cdot e^{\left(\frac{-z^S \cdot u \cdot \delta_3}{2}\right)} \\
j &= j^0 \cdot e^{\left(\frac{-z^R \cdot u \cdot \delta_1}{2}\right)} & k &= k^0 \cdot e^{\left(\frac{z^R \cdot u \cdot \delta_1}{2}\right)} \\
l &= l^0 \cdot e^{\left(\frac{z^R \cdot u \cdot \delta_3}{2}\right)} & m &= m^0 \cdot e^{\left(\frac{-z^R \cdot u \cdot \delta_3}{2}\right)} \\
\alpha &= \alpha^0 \cdot e^{\left(\frac{\left(z^C + z^R\right) \cdot u \cdot \delta_2}{2}\right)} & \beta &= \beta^0 \cdot e^{\left(\frac{-\left(z^C + z^R\right) \cdot u \cdot \delta_2}{2}\right)} \\
\gamma &= \gamma^0 \cdot e^{\left(\frac{z^C \cdot u \cdot \delta_2}{2}\right)} & \delta &= \delta^0 \cdot e^{\left(\frac{-z^C \cdot u \cdot \delta_2}{2}\right)} \\
\varepsilon &= \varepsilon^0 \cdot e^{\left(\frac{\left(z^C + z^S\right) \cdot u \cdot \delta_2}{2}\right)} & \zeta &= \zeta^0 \cdot e^{\left(\frac{-\left(z^C + z^S\right) \cdot u \cdot \delta_2}{2}\right)} \\
\eta &= \eta^0 \cdot e^{\left(\frac{\left(z^C + z^S + z^R\right) \cdot u \cdot \delta_2}{2}\right)} & \theta &= \theta^0 \cdot e^{\left(\frac{-\left(z^C + z^S + z^R\right) \cdot u \cdot \delta_2}{2}\right)}
\end{aligned}
\tag{22}
$$

For the eight-state carrier, principle of detailed balance combined with the Nernst equation leads to:

$$
e^{\left(\frac{V^{eq} \cdot F \cdot z^S}{R \cdot T}\right)} = \frac{\beta \cdot b \cdot g \cdot k \cdot \eta \cdot l \cdot h \cdot c}{\alpha \cdot d \cdot i \cdot m \cdot \theta \cdot j \cdot f \cdot a} \tag{23}
$$

Note that the exponential term in Equation 23 does not contain charge of the co-transported substrate R. This reflects the fact that the eight-state model has more degrees of freedom than the six-state model. Substrate S and R influxes via an eight-state carrier were defined as:

$$
\Delta S_i = f \cdot NES_i - g \cdot c^S{}_i \cdot NE_i \tag{24}
$$

$$
\Delta R_i = b \cdot NER_i - a \cdot c^R{}_i \cdot NE_i + j \cdot NESR_i - k \cdot c^R{}_i \cdot NES_i \tag{25}
$$

For the MntH protein, S substrate represents H^+ and R stands for the co-transported divalent metal ion.

Equations describing carrier models were numerically solved using Berkeley Madonna 8.0 software developed by Robert Macey and George Oster from the University of California at Berkeley and programmed by Tim Zahler[III]. Berkeley Madonna is a fast and convenient user-friendly program that numerically solves difference equations, systems of ordinary differential equations and discrete simulations. It offers a choice of four basic integration methods (1st order Euler algorithm, 2nd and 4th order Runge-Kutta algorithms and Rosenbrock algorithm) with adjustable parameters. For most of our models, Rosenbrock or 4th order Runge-Kutta algorithms were used. Berkeley Madonna software enables a fast and efficient adjusting of all model parameters using sliders, and easily produces two dimensional plots of any variables and parameters.

Several checks were performed to test the accuracy of each of our models. These included setting various rate constants or state occupancies to zero, checking that substrate influx inside the cell is equal to substrate efflux outside or vice versa, and testing that all conservation laws are observed.

When the effect of time-dependent voltage on carrier transport was simulated, oscillating voltage was added to the applied resting membrane potential value. Studied time-dependent voltage types include sine wave, sawtooth wave and triangle wave voltage, and voltage produced by ion channels and excitable cells. Sawtooth wave voltage was simulated according to equation:

$$V = t \bmod P \qquad (26)$$

where t represents time and parameter P describes both the frequency and amplitude of applied sawtooth wave voltage (with an increasing value of P, sawtooth wave frequency is decreasing and its amplitude is increasing).

Triangle wave voltage was simulated according to the following formula:

$$V = 2 \cdot A \cdot \left(1 - \frac{t \bmod R}{R}\right) \text{ when } t \bmod R \geq \frac{R}{2}$$
$$V = 2 \cdot A \cdot \left(\frac{t \bmod R}{R}\right) \text{ when } t \bmod R < \frac{R}{2} \qquad (27)$$

where t stands for time, A is the amplitude of the triangle wave and parameter R is reciprocally proportional to its frequency.

[III] www.berkeleymadonna.com

Voltage time course produced by ion channels was modelled as random square wave voltage with adjustable parameters describing the probability of a channel to remain closed or open. The effect of two and more channels was simulated as a superposition of a number of random square waves. Action potential voltage was simulated with the help of model examples that are a part of the Berkeley Madonna software.

In our simulations, a certain value needed to be assigned to all model parameters. Because little is known about real rate constant values or intracellular metal ion concentrations, not the numeric values of these parameters but their ratios were adjusted to desired values. All model parameter values can be regarded as being expressed in standard units, e.g. M for concentration and s^{-1} or $(Ms)^{-1}$ for rate constants (depending on the reaction type).

3 Results and discussion

3.1 Experimental results

Unless stated otherwise, all experimental data shown were calculated as average values of at least three experimental results obtained from different bacterial cultivations, and error bars represent standard deviation.

3.1.1 Membrane potential of *E. coli* cells

To find out whether the overexpression of *MNTH* influences membrane potential of *E. coli* cells, staining by the diS-C_3(3) dye was measured in strains containing and lacking the MntH protein. In order to find optimal experimental conditions, we tried out various concentrations of diS-C_3(3), and found the concentration of 0.1 μM to be sufficient for the cells to be stained (at optical density 0.2). For each sample, emission intensity ratio was measured five times every three minutes and staining curves were constructed (Figure 10). Staining by diS-C_3(3) measured 15 minutes after the addition of the dye was then compared for six bacterial strains and two buffer *pH* values (Figure 11 and Figure 12).

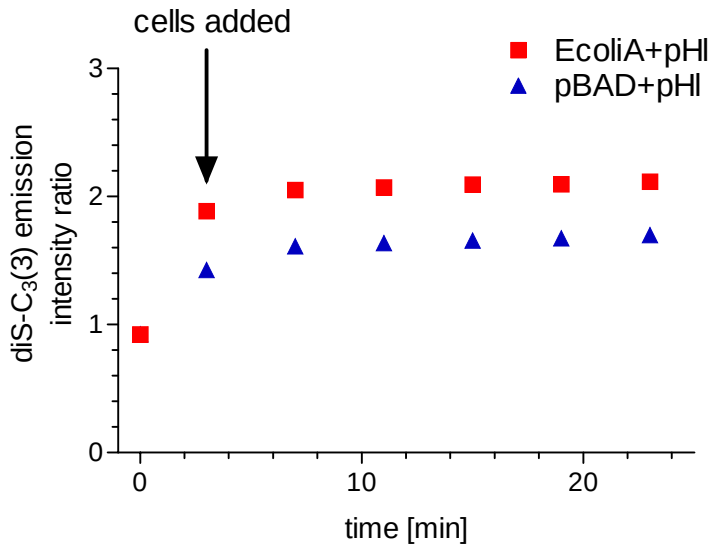

Figure 10 – A typical example of staining curves obtained at pH_o 5.5 for EcoliA+pHl and pBAD+pHl strains.

At an external *pH* (pH_o) value of 4.7, EcoliA cells are stained more than pBAD cells (Figure 11). This difference was found to be statistically significant (P-value<5%). However, differences in staining between EcoliA and pBAD cells are not significant at pH_o 5.5. Because diS-C_3(3) is distributed inside the cell according to its membrane potential, results presented in Figure 11 suggest that EcoliA cells have a slightly more negative membrane potential than pBAD cells. Since the only difference between these two strains is the presence of MntH protein in EcoliA cells and its absence in pBAD cells, our results indicate that the presence of this protein shifts membrane potential towards more negative values. However, our data do not contain any information about the size of this effect. The reason of the observed hyperpolarisation of EcoliA cells is not clear. According to the measurements of pH_i of these two strains ([61] and Chaloupka,R., Urbánková, E. – unpublished results), EcoliA strain has lower intracellular *pH* than pBAD in pH_o 4.7 (the difference is 0.2 *pH* units, but statistically significant). The natural explanation of this *pH* difference would be that, under given conditions (*pH* 4.7 outside), MntH uncouples the proton-motive force on bacterial plasma membrane by mediating proton uptake (uniport of protons). But why would bacteria under these conditions have higher membrane potential? The only way how to explain this is to suppose that the MntH-mediated proton flux is compensated by a flow of other ion, so that the transport is electroneutral. Then, internal *pH* would be lower, but the membrane potential would not – it could be even higher, provided that the bacteria would upregulate the activity of the respiratory chain. The nature of this counter-flux (if there is any) is not clear – it could

be mediated by MntH, or other transport protein. There have been speculations that MntH could transport certain anions as well [24], but they have not been confirmed yet.

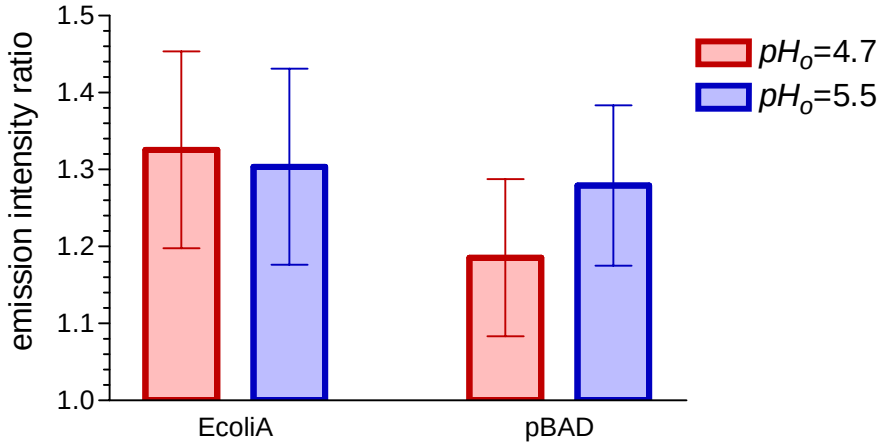

Figure 11 – Ratio of the emission intensity measured at 580 nm and 560 nm 15 minutes after the addition of 0.1 μM diS-C_3(3) to bacterial strains without pHluorin

EcoliA+pHl cells are stained more than pBAD+pHl cells at both external *pH* values (Figure 12). Mutant cells D34G and N401G are stained very similarly and both are stained more at pH_o 4.7. Comparing Figure 11 and Figure 12 reveals that bacterial strains without pHluorin are stained less than their pHluorin-containing analogues. Therefore, *pHLUORIN* expression either shifts the cell membrane potential value, influences fluorescence of diS-C_3(3), or alters some other characteristics that make cell staining more favourable.

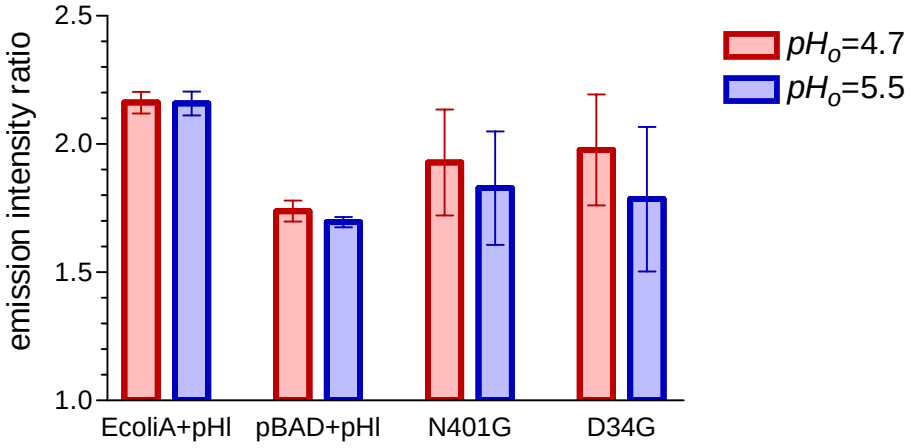

Figure 12 – Ratio of the emission intensity measured at 580 nm and 560 nm 15 minutes after the addition of 0.1 μM diS-C_3(3) to bacterial strains expressing *pHLUORIN*

3.1.2 Metal ion transport

The main aim of our experiments was to measure the effects of divalent ions (Mn^{2+}, Cd^{2+} and Zn^{2+}) on the membrane potential, ideally simultaneously with the measurement of intracellular *pH* changes. Because the MntH carrier is highly electrogenic, we expected the negative cell membrane potential to depolarise (at least transiently) due to the transport of positively charged ions into the cell. Such a depolarisation caused by MntH-mediated metal transport has already been observed on right-side-out vesicles made of *E. coli* cells [62]. The question was whether the same effect can be observed on intact bacterial cells.

diS-C_3(3) emission intensity ratios were measured five times every 4 minutes after the addition of $MnCl_2$, $CdCl_2$ or $ZnCl_2$ at a final concentration of 30 μM or 300 μM. Moreover, fluorescent emission intensity ratios for pHluorin were measured for the N401G and D34G strains to monitor the intracellular *pH* responses to the addition of diS-C_3(3) and to metal ion uptake accompanied by proton influx. Figures 13 – 16 show diS-C_3(3) emission intensity ratios measured 16 minutes after the addition of metal ions (R_a) as a percentage of the original emission intensity ratio that was measured without metal ions (R_b):

$$R = \frac{R_a - R_{ref}}{R_b - R_{ref}} \cdot 100\% \qquad (27)$$

where R_{ref} stands for the value of the emission intensity ratio for the free dye that was used as a reference state.

Monitoring membrane potential changes at pH_o 4.7 revealed that both Mn^{2+} and Cd^{2+} cause membrane potential depolarisation in EcoliA cells that is dependent on the metal ion concentration. However, no significant effects on membrane potential were observed at pH_o 5.5 (Figure 13 and Figure 14). Because previous experiments performed on EcoliA cells confirmed that transport via the MntH protein occurs in these conditions[IV], our results can be explained by the fact that the cell is able to immediately compensate for the influx of cations and this is why membrane potential remains unchanged (at the time resolution of our experiments).

[IV] Chaloupka, R., Urbánková, E. - unpublished results

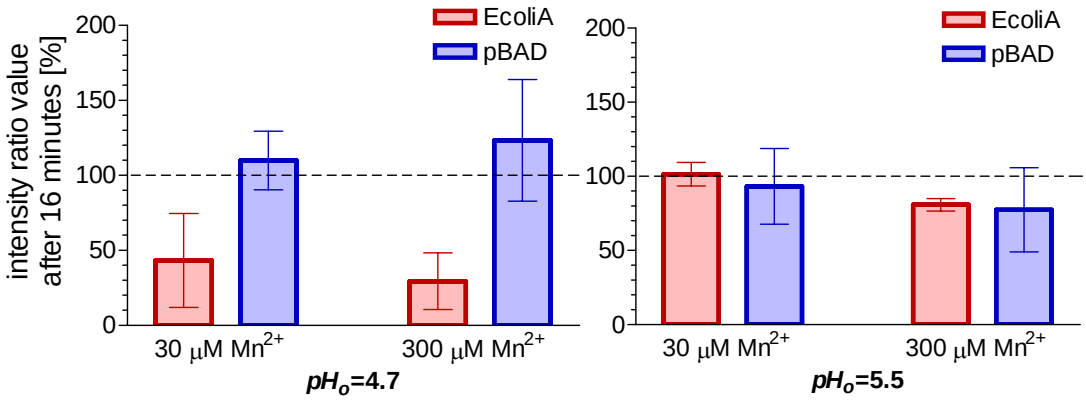

Figure 13 – Membrane potential depolarisation caused by Mn^{2+} measured 16 minutes after the addition of 30 μM or 300 μM $MnCl_2$ to EcoliA and pBAD cells. As a result of membrane potential depolarisation, intensity ratios obtained for EcoliA cells at pH_o 4.7 decreased to approximately 40% of their original value upon the addition of Mn^{2+}. Intensity ratios at pH_o 4.7 measured for pBAD cells that serve as a negative control stayed almost the same when Mn^{2+} was added. This confirms that Mn^{2+} transport observed in EcoliA cells occurred via the MntH protein. According to our expectations, Mn^{2+} induced membrane potential depolarisation is bigger when Mn^{2+} concentration is higher. Only a small effect of Mn^{2+} on membrane potential is observed in both EcoliA and pBAD cells at an external *pH* of 5.5.

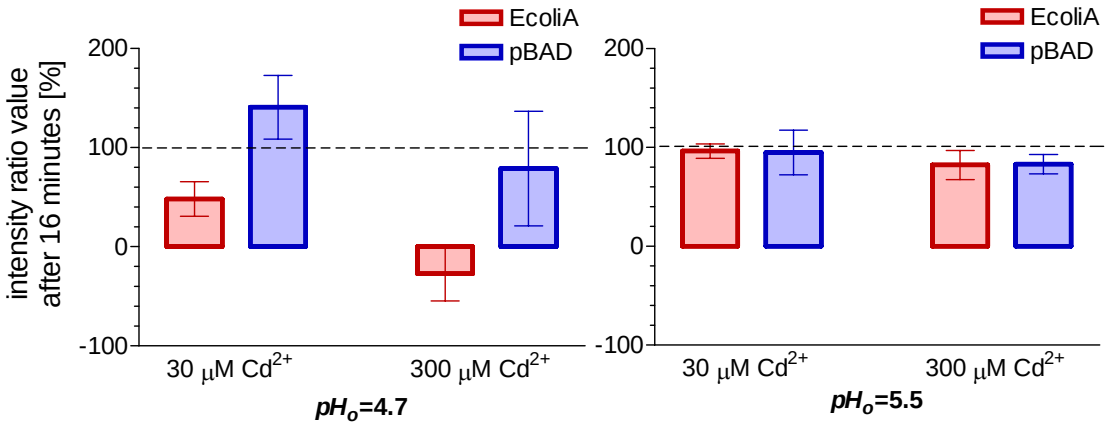

Figure 14 – Membrane potential depolarisation caused by Cd^{2+} measured 16 minutes after the addition of $CdCl_2$ to EcoliA and pBAD cells. At a pH_o of 4.7 and metal ion concentration of 300 μM, Cd^{2+} uptake is higher than Mn^{2+} uptake in EcoliA cells. However, membrane potential depolarisation effects at pH_o 4.7 are approximately the same for both metal ions when their concentration is 30 μM. Similarly to Mn^{2+} transport, Cd^{2+} uptake in EcoliA cells is considerably smaller at higher pH_o values.

While the mutant strain N401G exhibited membrane potential depolarisation upon the addition of Mn^{2+} when pH_o=5.5 and upon the addition of Cd^{2+} for both pH_o values, membrane

potential in D34G cells remained unchanged when metal ions were added (Figure 15 and Figure 16). This is in agreement with previous results [61], which reported a loss of transport function of this mutant.

No significant membrane potential depolarisation was observed in EcoliA, pBAD, N401G or D34G cells after the addition of 30 μM or 300 μM Zn^{2+} (data not shown).

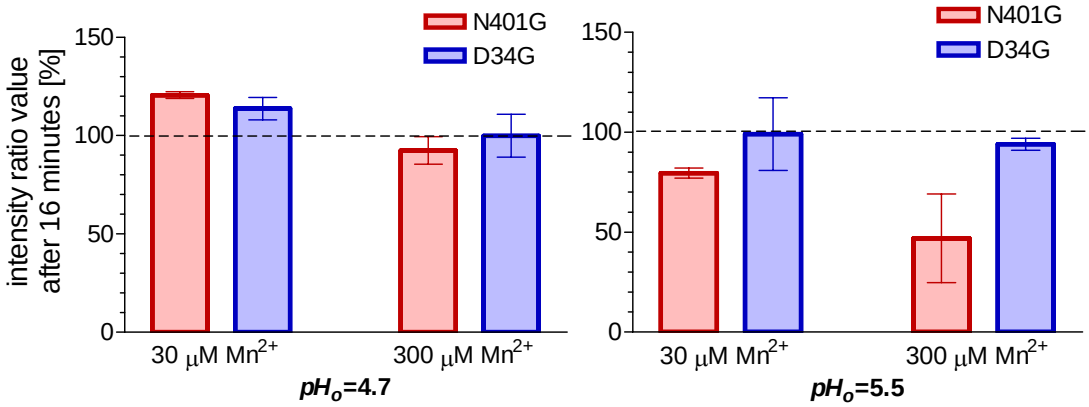

Figure 15 – Membrane potential depolarisation caused by Mn^{2+} measured in N401G and D34G cells 16 minutes after the addition of $MnCl_2$. Unlike EcoliA cells, N401G cells seem to transport more Mn^{2+} at pH_o 5.5 than at pH_o 4.7. No significant Mn^{2+} membrane potential shifts are observed in D34G cells.

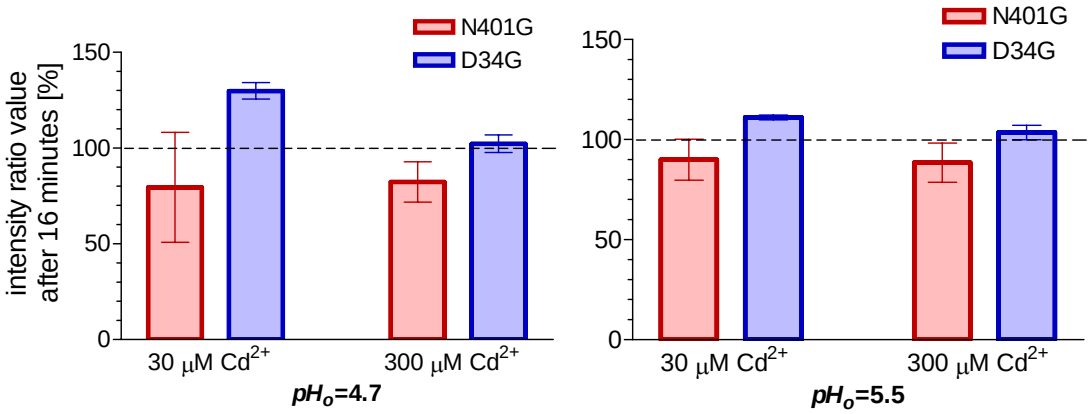

Figure 16 – Membrane potential depolarisation caused by Cd^{2+} measured in N401G and D34G cells 16 minutes after the addition of $CdCl_2$. Cd^{2+} is shown to be transported by N401G cells at both external *pH* values while D34G cells do not exhibit any signs of Cd^{2+} transport.

Simultaneous measurements of diS-C_3(3) and pHluorin emission intensity ratios were performed in N401G and D34G cells to test the possibility of measuring changes in membrane potential and intracellular *pH* at the same time. However, pH_i changes could be

monitored only qualitatively. To see their size, a pHluorin calibration curve for cells containing diS-C_3(3) would be needed. Because using standard calibration curves for *E. coli* cells did not lead to any reasonable results, the presence of diS-C_3(3) in the cell seems to affect the fluorescence of pHluorin. Results of the pHluorin emission intensity measurements show that, due to the co-transport of protons together with metal ions via the MntH protein, pH_i increased after the addition of metal ions to N401G cells. No effects on the pH_i value were observed in D34G cells upon the addition of metal ions, which confirms our previous observation that MntH is not active in this strain.

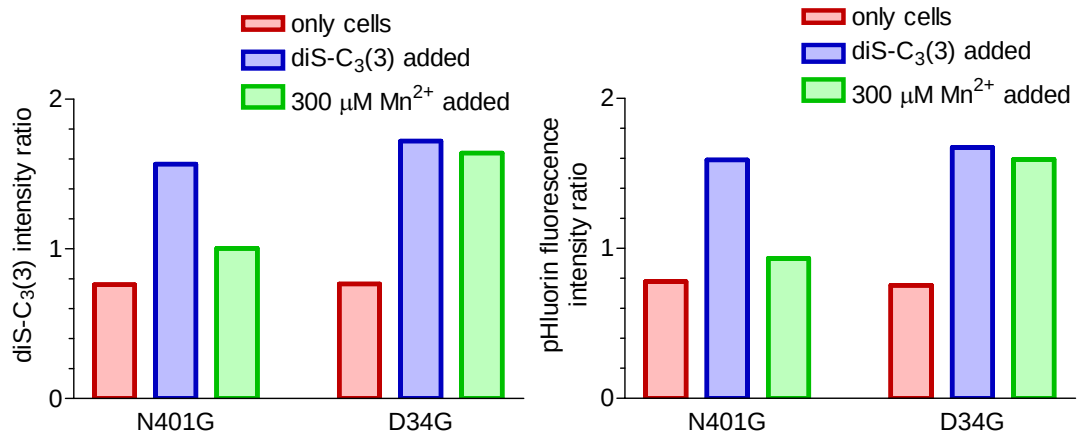

Figure 17 – An example of simultaneous diS-C_3(3) and pHluorin emission intensity measurements obtained at pH_o=5.5. Results shown were measured 15 minutes after the addition of diS-C_3(3) and 20 minutes after the addition of 300 μM $MnCl_2$. Higher pHluorin emission intensity ratio corresponds to higher pH_i values. Note that the pHluorin intensity ratio remarkably increases upon the addition of diS-C_3(3).

3.2 Results of mathematical simulations

We theoretically studied the kinetics of three different carrier schemes, starting with the simplest case of an electroneutral simple and symmetric four-state uniporter, continuing with general four- and six-state carrier models and ending up exploring the eight-state model introduced for the Nramp2 transporter in [1]. We varied different model parameters including membrane potential, rate constants, carrier and substrate charges and substrate concentrations to explore their effects on substrate flux. Results obtained for a charged carrier were usually compared to results obtained under an assumption of uncharged carrier in order to demonstrate the effect of incorporating the influence of carrier charge on carrier reorientation and therefore on substrate transport.

3.2.1 Voltage effects on electroneutral carriers

The first and simplest model system we studied was a simple and symmetric electroneutral four-state uniporter described by Equation 4 and depicted in Figure 2. Initial binding and releasing rate constant values (before voltage was switched on) were set to a_i^0=1, a_o^0=1, b_i^0=1 and b_o^0=1, and initial reorientation rate constants values to g_i^0=200, g_o^0=200, h_i^0=200 and h_o^0=200. All initial carrier state occupancies (NE_i^0, NE_o^0, NES_i^0 and NES_o^0) were set to ten. Substrate was uncharged because we wanted the uniport to be electroneutral; carrier charge was set to one. Fractions of membrane potential influencing substrate binding or releasing inside the cell, empty or loaded carrier reorientation, and substrate binding or releasing outside were set as δ_1=0.1, δ_2=0.8 and δ_3=0.1, respectively. Substrate concentration outside was hundred times higher than inside (c^S_o=100 and c^S_i=1). Because the exponential parts of all binding and releasing rate constants in Equation 10 equal one when z^S=0, only reorientation steps are influenced by voltage in an electroneutral uniporter.

First of all, the effect of carrier charge on substrate influx was studied (Figure 18). Carrier charge was found to determine the voltage range where substrate influx is observed. Within this range, substrate influx decreases with the growing absolute value of carrier charge.

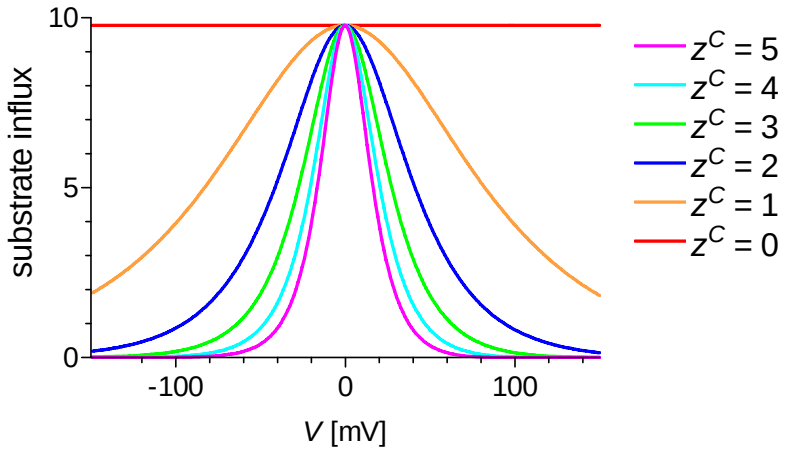

Figure 18 – The effect of carrier charge on substrate influx for a simple and symmetric electroneutral four-state carrier. When carrier charge equals zero, substrate flux is not influenced by the value of applied voltage and has its highest possible value. Positive carrier charge leads to a reduction of substrate influx at non-zero membrane potential values. Substrate flux is decreasing with the increasing absolute value of carrier charge for all membrane potential values except zero. Similar results were obtained for negative carrier charges (data not shown).

Next, we concentrated on the effects of substrate concentration outside the cell on substrate influx (Figure 19). No effects were observed when substrate concentration was the same on both sides of the membrane. Apart from that, the value and direction of substrate flux was influenced by the actual substrate concentration gradient, and the absolute value of substrate influx was decreasing with increasing absolute values of membrane potential.

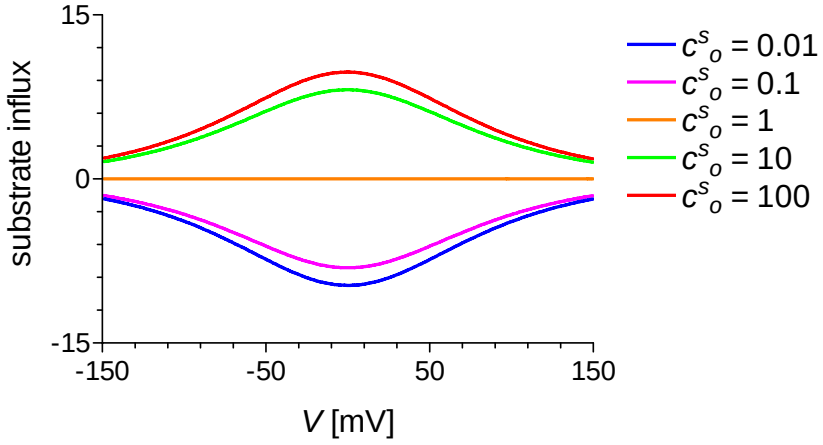

Figure 19 – Effects of outside substrate concentration on substrate influx for a simple and symmetric electroneutral carrier; substrate concentration inside the cell equals one. Substrate influx gets higher as outside substrate concentration increases; in the case of a negative concentration gradient, substrate influx reaches negative values. This means that substrate is not transported into the cell but is carried out. When a concentration gradient is applied, the absolute value of substrate influx reaches its maximum at zero membrane potential and is slowly decreasing with growing absolute values of applied voltage.

As a next step, we varied the parameter δ_2 describing the fraction of membrane potential affecting carrier reorientation (Figure 20). Our results indicate that an electroneutral carrier is not influenced by voltage when δ_2 is zero. This can be easily deduced from Equation 10 where all exponential terms multiplying initial values of rate constants equal one when substrate charge z^S and membrane potential fraction δ_2 are zero, and therefore no rate constants are voltage dependent. In the case of a non-zero δ_2 value, substrate influx is decreasing with growing absolute membrane potential values. The more is reorientation influenced by voltage (i.e. the bigger is δ_2), the lower value reaches substrate influx when membrane potential has a non-zero value. For an electroneutral uniporter, curves in Figure 20 are similar to curves in Figure 18 because both describe the fact that the bigger the carrier charge is, the more is substrate transport restricted at higher negative or positive membrane potential values. However, Figure 20 would look differently for an electrogenic carrier as it would also include the effect of substrate charge on carrier reorientation (see Chapter 3.2.2).

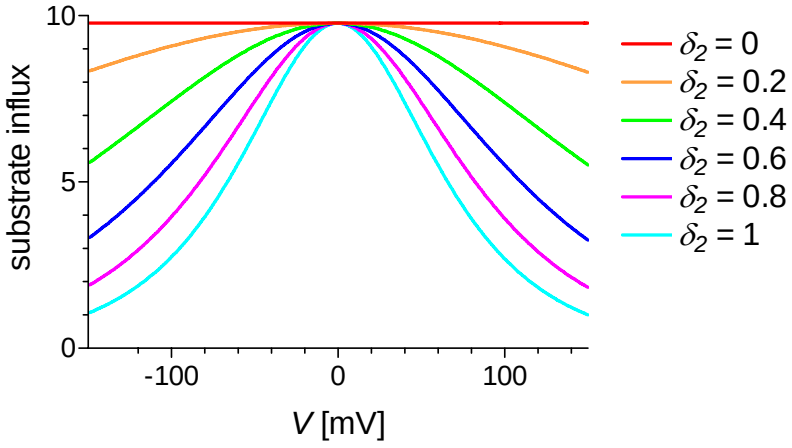

Figure 20 – Substrate influx in a simple and symmetric electroneutral carrier simulated for various values of parameter δ_2 describing the fraction of membrane potential that affects reorientation steps

Our next goal was to find out how does the amplitude and frequency of oscillating electrical fields influence transport mediated by electroneutral carriers. Such time dependent electrical fields can be a result of the presence of ion channels or excitable cells in the cellular membrane. Moreover, some experiments such as voltage clamp allow us to apply other types of time dependent voltage such as sine wave, sawtooth wave or a triangle wave voltage to study transport under these artificial conditions.

Opening and closing of ion channels present in the membrane cause oscillations in the local membrane potential, which can be sensed by a carrier when ion channels are situated in its close vicinity. Total voltage sensed by the carrier was simulated by adding this channel voltage to the constant resting membrane potential value describing membrane potential when no channels are present in the membrane. Substrate influx at a given voltage was calculated as an average value of substrate influx over a time interval of 100 s that is much bigger than the average time interval during which a channel remains in an open or closed conformation. Our data suggest that substrate influx is considerably influenced by voltage changes produced by ion channels (Figure 21). For example, substrate influx is activated by the presence of an ion channel in the membrane at a physiological resting membrane potential value of -80 mV; this effect is even bigger when more channels are situated close to the carrier. The effect of ion channels on substrate influx can be explained by the fact that their opening and closing shifts the average voltage sensed by the carrier depending on the frequency of the channel conformation changes.

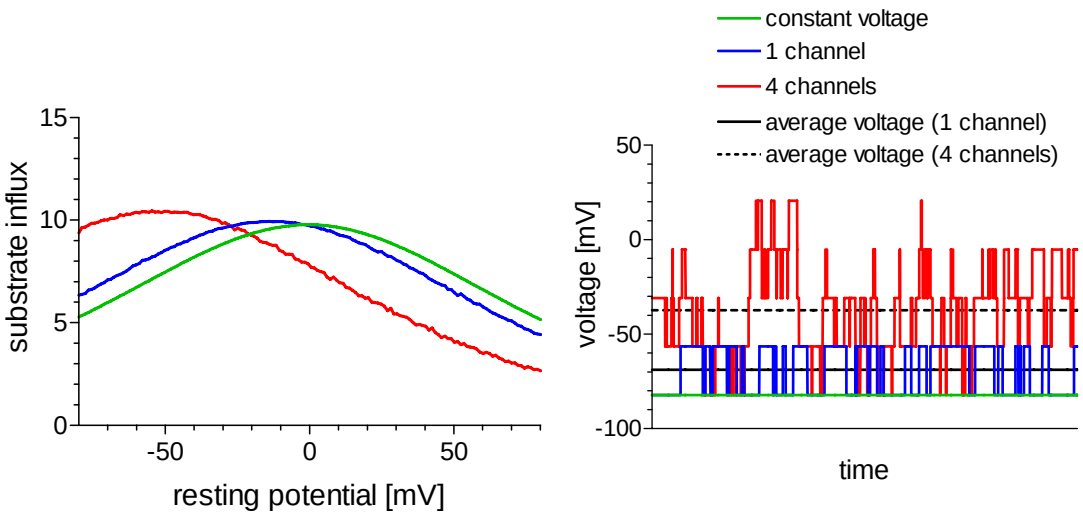

Figure 21 – The effect of opening and closing of ion channels on the mean value of substrate influx at different resting membrane potential values; and the time course of voltage sensed by the carrier when zero, one and four channels are present in the membrane

Next, the influence of carrier transport by a more theoretical types of applied voltage – a sawtooth wave (Figure 22 a)), a triangle wave (Figure 22 b)) and a sine wave (Figure 23) – was studied. It was shown that both the parameter *P* of a sawtooth wave (defined in Equation 26) and the amplitude of a triangle wave have a profound effect on substrate influx via an electroneutral carrier. When sine wave voltage with a frequency 0.1 s^{-1} was applied, substrate flux was influenced by its amplitude (Figure 23). We also simulated the influence of the presence of excitable cells such as pacemaker cells on substrate influx (Figure 24). Results presented in Figure 21 – Figure 24 show that even an electroneutral carrier is considerably influenced by the time course of applied voltage. For all studied types of oscillating voltage, an optimal frequency or amplitude where substrate influx reaches its maximum can be found. For the triangle and sawtooth waves, substrate influx is maximal when voltage is constant and decreases with increasing frequency of the oscillating membrane potential. However, the optimal amplitude of the sine voltage is different from zero, suggesting that a sine wave with favourable parameters could stimulate substrate influx. Interestingly, substrate influx is induced by the growing frequency of action potential produced by excitable cells.

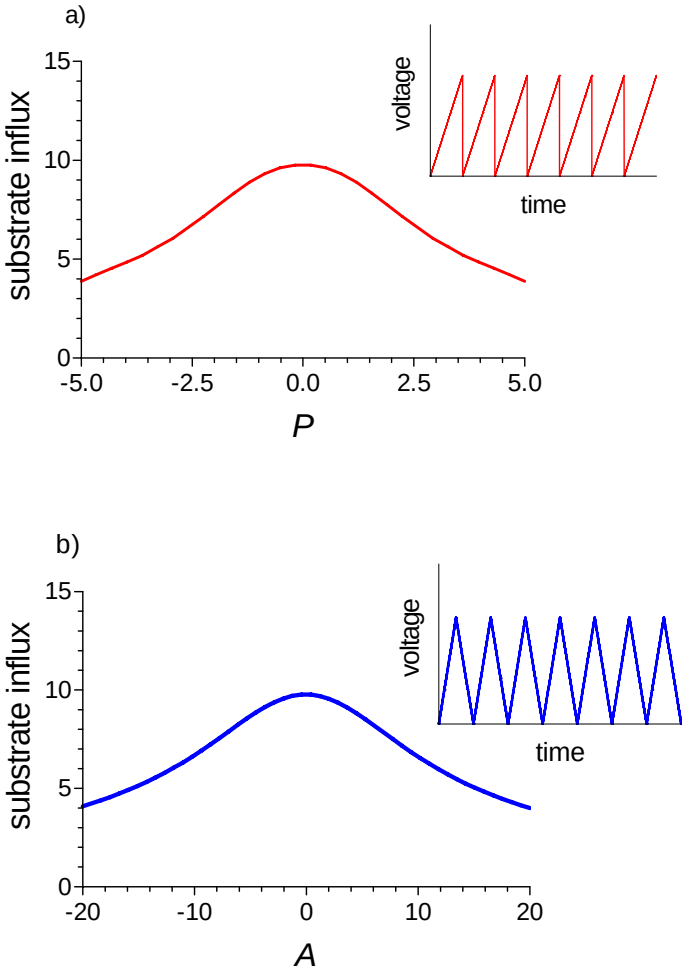

Figure 22 – a) The effect of sawtooth wave characteristics on substrate influx, and the time course of applied sawtooth wave voltage b) The effect of triangle wave amplitude on substrate influx, and the time course of applied triangle wave voltage

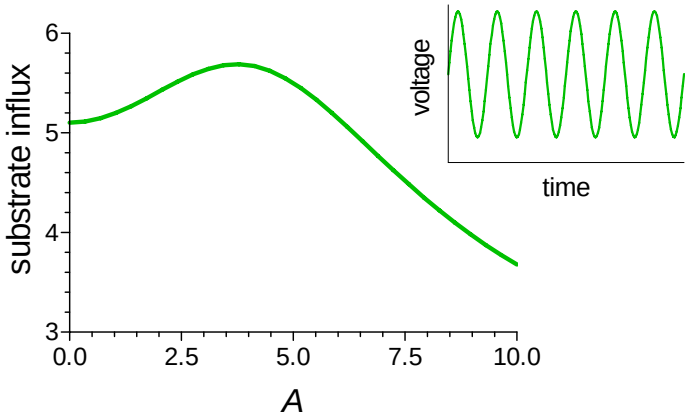

Figure 23 – The effect of sine wave amplitude *A* on substrate influx, and the time course of applied sine wave voltage

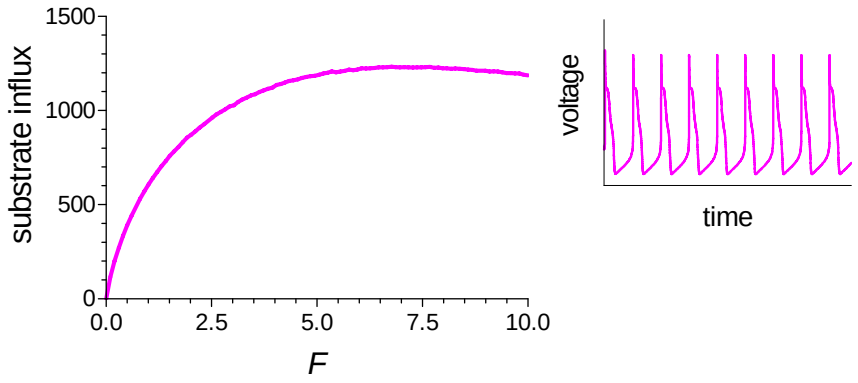

Figure 24 – Action potential frequency effect on substrate influx (parameter F is proportional to the frequency of applied action voltage), and the time course of applied action potential voltage

Our theoretically obtained results could be further verified in transport experiments such as voltage clamp (combined with another method to measure transport mediated by an electroneutral carrier) where changing the parameters of applied oscillating voltage should lead to a considerable change in substrate influx. These voltage clamp experiments were performed in the laboratory of Dr. Bernhard Schmitt at the University of Otago.

3.2.2 Voltage effects on general four-state carriers

A general electrogenic four-state carrier with voltage dependent rate constants was simulated according to Equations 8 and 10 where initial rate constant values were set, in order to avoid simplicity[V] of the carrier, as following: a_o^0= 0.02, b_i^0=4.36, b_o^0=0.08, g_i^0=0.64, g_o^0=0.98, h_i^0=0.14 and h_o^0=0.04[VI]. Rate constant a_i was calculated from Equation 14 to ensure that the principle of detailed balance is observed. Substrate charge was set to one and all initial state occupancies (NE_i^0, NE_o^0, NES_i^0 and NES_o^0) were ten. Parameters describing voltage effects on binding, releasing and reorientation steps were set to the following values: δ_1=0.1, δ_2=0.8 and δ_3=0.1. Simulations were performed with two carrier charge values (one and zero) so as to compare the situation when reorientation rate constants are influenced by carrier charge (z^C=1) with the situation when the effect of carrier charge on carrier transport is not considered (this leads to the same results as the condition z^C=0). Final values of all rate constants were set to be the same for both values of carrier charge at a membrane potential of -80 mV so as to keep final carrier state occupancies at this voltage unchanged. This was achieved by changing the initial values of reorientation rate constants to a_o^0= 0.07, b_i^0=1.21

[V] See Chapter 1.1.2.1
[VI] All listed values were rounded to two decimal digits.

and b_o^0=0.27[VII] when z^C=0. These two model systems were used to study voltage effects on carrier transport under various conditions (e.g. variable substrate concentration or substrate charge).

First of all, we studied the dependence of carrier transport on substrate concentration for both carrier charge values when V=-80 mV (Figure 25) and when membrane potential was varied (Figure 26). At a membrane potential of -80 mV, substrate influx becomes saturated for high outer substrate concentrations (Figure 25). This behaviour is similar to Michaelis-Menten kinetics (Equation 1) although we do not study initial substrate fluxes as there is already some substrate inside the cell in the beginning of our simulations (at a low c^S_o concentration, there is even observable substrate efflux). Incorporating the carrier charge dependence into our model narrows the voltage range where substrate influx occurs (Figure 26). This is evident mainly at highly negative membrane potential values where substrate influx is higher when z^C=0 than when z^C=1. Also substrate influx at positive membrane potentials calculated when z^C=0 remarkably exceeds substrate influx when z^C=1.

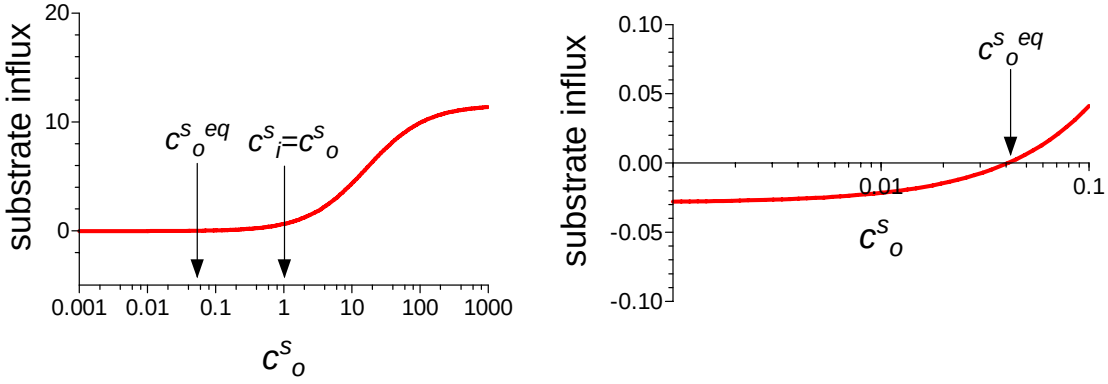

Figure 25 – Effect of substrate concentration outside the cell (in a logarithmic scale) on substrate influx at a resting membrane potential of -80 mV; substrate concentration inside the cell equals one and carrier charge is either one or zero (both values lead to the same result due to our choice of rate constants). Equilibrium outside substrate concentration calculated from Equation 5 as $c^{S}_{o}{}^{eq}$=0.044 (at -80 mV) is marked in both graphs and represents the minimal c^S_o value sufficient for the transport of substrate into the cell. Substrate influx becomes slightly negative when c^S_o<$c^{S}_{o}{}^{eq}$ which means that substrate is transported out of the cell.

[VII] All listed values were rounded to two decimal digits.

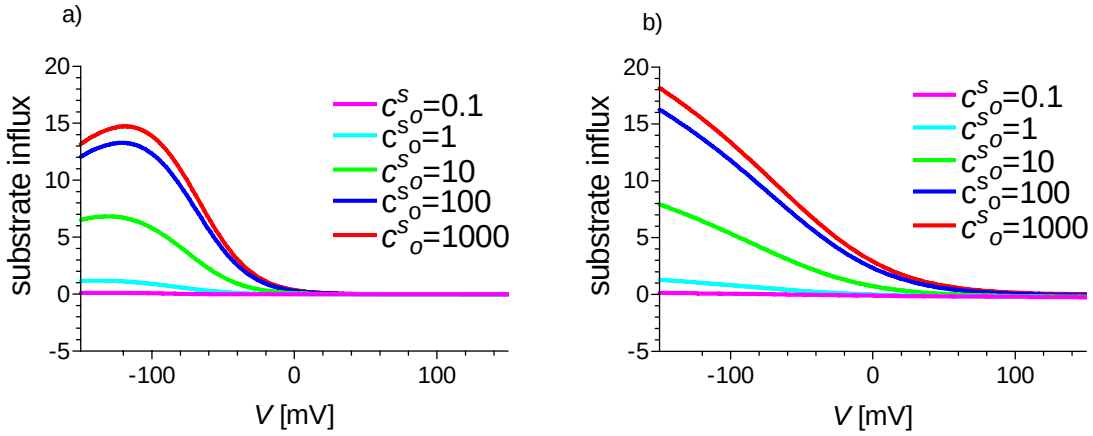

Figure 26 – Voltage dependence of substrate influx at various substrate concentrations outside the cell (while inside substrate concentration equals one) a) when carrier charge equals one b) when carrier charge effects on carrier transport are not considered. The bigger is the electrochemical concentration gradient towards the inside, the more substrate is transported into the cell. Significant uptake of a positively charged substrate occurs mainly at negative membrane potential values. The optimal resting membrane potential range where substrate flux reaches its maximum at a given substrate concentration is approximately -115 mV to -140 mV (the exact value depends on c^S_o) (Panel a)); substrate influx for a given c^S_o decreases when membrane potential differs from its optimal value. When effects of carrier charge are not considered, substrate influx keeps on increasing (in the studied voltage range) as membrane potential becomes more negative (Panel b)) and is higher at positive membrane potential values when z^C=0 than when z^C=1. The bigger is the substrate concentration gradient, the higher membrane potential value is needed to suppress substrate influx at positive membrane potential values.

Because both substrate charge and carrier charge are a part of exponential terms describing voltage dependence of rate constants in Equation 10, they significantly affect substrate flux when applied voltage is different from zero. Compared to a simple and symmetric electroneutral carrier, whose substrate influx dependence on carrier charge can be found in Figure 18, the situation is more complicated for an electrogenic carrier (Figure 27). Electrogenicity of the carrier causes the maximal substrate influx values and the optimal voltage values where influx reaches its maximum to shift with changing carrier charge. More specifically, when the absolute value of carrier charge is rising, peaks describing substrate influx become narrower, and the optimal membrane potential value shifts towards zero. While negative carrier charge enables influx of a positively charged substrate at positive membrane potential values, positive carrier charge facilitates influx when membrane potential is negative. Because the charge of a carrier may depend on the *pH* of its surroundings, Figure 27 can also be interpreted as a description of the *pH* effect on carrier transport. Thus, carrier

transport can be switched on or off at a certain voltage by altering the surrounding *pH*, and interplay between *pH* and membrane voltage is able to finely tune the transport rate.

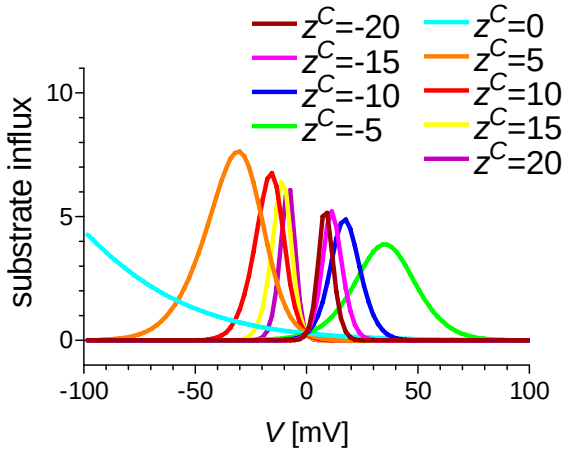

Figure 27 – Voltage dependence of substrate influx at various carrier charges for a general electrogenic four-state carrier

The influence of substrate charge on substrate influx when z^C=1 (Figure 28 a)) and when z^C=0 (Figure 28 b)) was further studied. Interestingly, while curves describing substrate influx when z^C=0 are symmetric around zero membrane potential, curves calculated when z^C=1 are highly asymmetric. Carrier charge effects seem to reduce influx of a positively charged substrate at negative membrane potential values, and enhance negatively charged substrate influx when membrane potential is positive (for example, when z^S=-5, substrate influx at 80 mV equals approximately 40 when z^C=1, and only 28 when z^C=0). Analogically, a negatively charged carrier supports the influx of a positively charged substrate when membrane potential is negative and causes the influx to decrease at positive membrane potential values (data not shown).

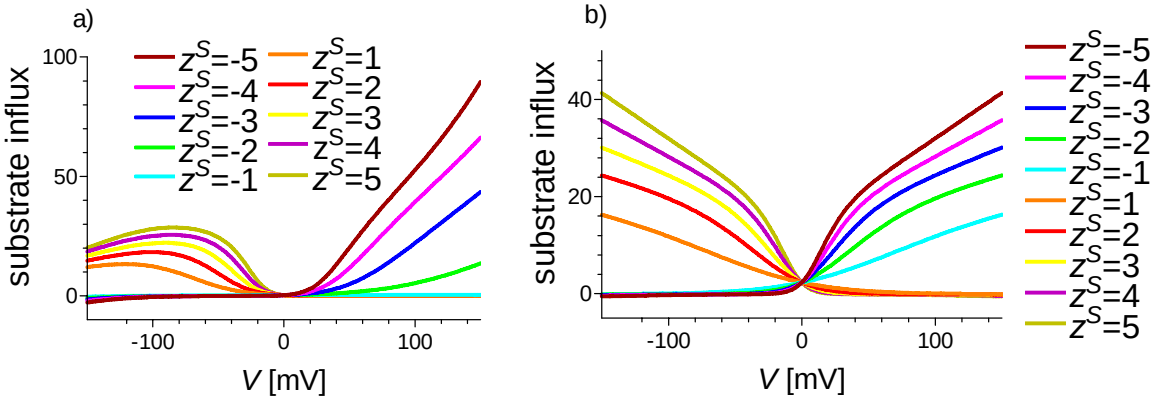

Figure 28 – Voltage effects on substrate influx for different values of substrate charge for a general electrogenic four-state carrier a) when z^C=1 b) when z^C=0. No positively charged substrate is transported into the cell when positive cell membrane potential is higher than the equilibrium potential in Equation 14, and no negatively charged substrate is transported into the cell when the negative membrane potential value is lower than the corresponding equilibrium potential. When voltage and substrate charge have opposite signs, substrate influx becomes higher with the increasing absolute value of substrate charge.

As a next step, we focused on the relative importance of ion-well and electroconformational coupling effects – i.e. the significance of the membrane potential fraction δ_2 that affects reorientation of both loaded and unloaded carrier states from the outside to the inside of a cell and vice versa. For our set of rate constants, substrate charge and concentrations, and at a physiological membrane potential value of -80 mV, substrate influx has its highest value when δ_2=1 and is decreasing with decreasing δ_2 for both studied carrier charges (Figure 29). Therefore, in a certain voltage range, substrate influx is maximal when only carrier reorientation steps are influenced by voltage and substrate binding and releasing steps are not voltage dependent.

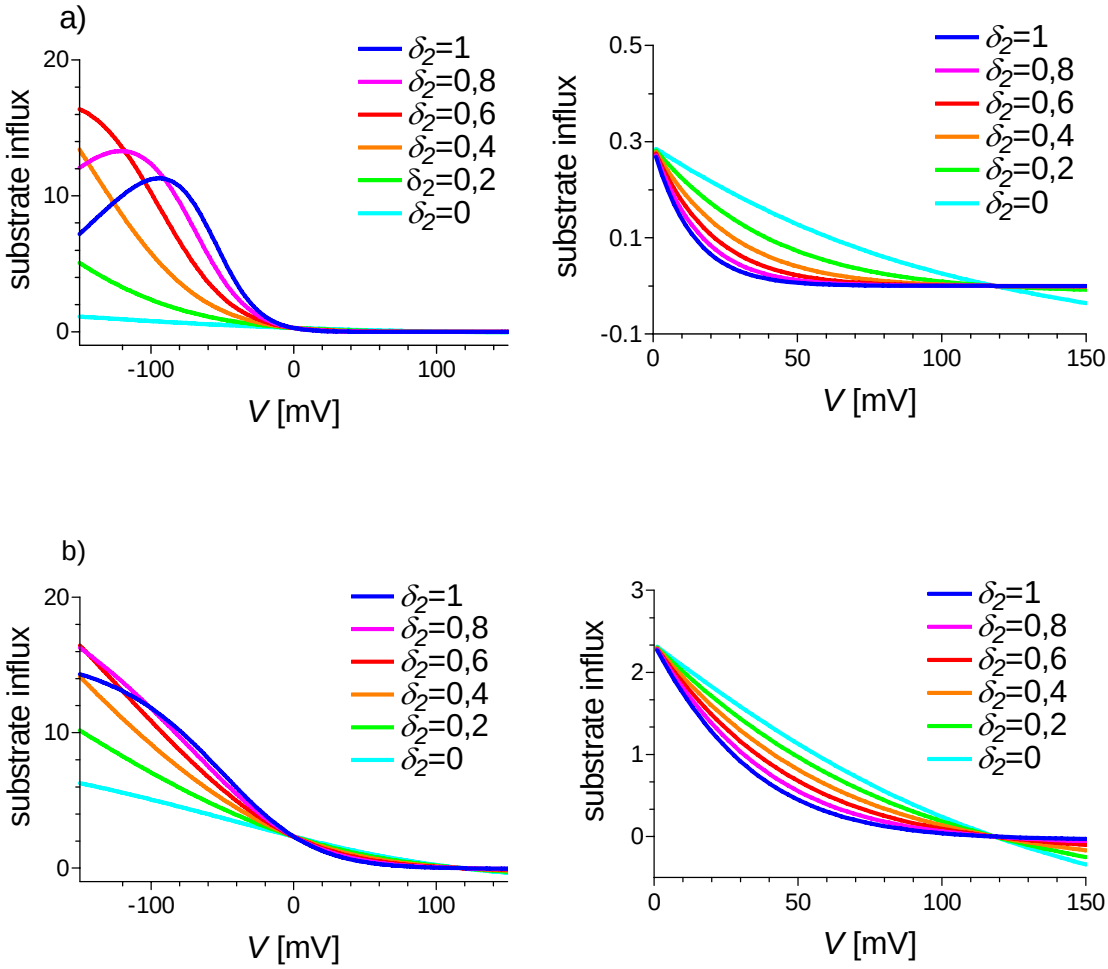

Figure 29 – Substrate influx versus applied voltage for various values of parameters δ_2 describing the amount of voltage dependence of reorientation steps in carrier transport a) when z^C=1 (δ_2 represents the membrane potential fraction sensed during carrier reorientation not only by the substrate but also by the charged carrier) b) when z^C=0 (δ_2 is the membrane potential fraction sensed during reorientation by the substrate). Values of membrane fractions δ_1 and δ_3 were chosen for each data set so as they obey Equation 7 and equal each other. When carrier charge equals one, substrate influx starts to decrease at a certain voltage value that is δ_2 dependent; within our studied voltage range this effect can be observed when δ_2 is 1 and 0.8. A similar effect probably occurs when z^C=0 but the voltage interval where substrate influx is growing is wider than the voltage range we studied (a similar effect of a positive carrier charge narrowing the voltage range where transport can be observed was shown in Figure 26). When membrane potential is positive, influx (or efflux, depending on the actual voltage value) of a positively charged substrate is higher for lower δ_2 values. Substrate influx becomes negative at a certain voltage that can be calculated from Equation 14 (approximately 116 mV).

3.2.3 Voltage effects on a general six-state symporter

Our ultimate goal was to explore the properties of several different transport schemes that could provide a simplified description of the MntH protein. Although the four-state

carrier model enabled us to describe some effects connected with carrier and substrate charge, a more complicated model has to be introduced to study secondary active symport. Under the assumption that both substrates are bound simultaneously, even the four-state carrier scheme could be regarded as a simplified scheme of a symporter, but a six-state scheme must be introduced to simulate the consecutive binding of co-transported substrates in a given order. In addition, the six-state scheme explains the slip of the "driving" substrate observed for MntH [35]. The general six-state symporter model can be regarded as a simplified model of the MntH transporter when we suppose that substrate S in Figure 3 a) represents H^+ and substrate R stands for Fe^{2+} or other divalent metal ion. We chose the outer conditions to represent a typical situation for a secondary active symporter – concentration of the "driving" substrate S was higher outside the cell than inside and substrate R concentration was higher inside the cell (c^S_i=1, c^S_o=100, c^R_i=100 and c^R_o=1). Our goal was to find a set of initial rate constant values that would enable us to see how the influx of substrate S (H^+ in MntH) causes substrate R (Fe^{2+}) influx against its electrochemical potential.

Kinetics of a general six-state symporter was simulated according to Equations 16 and 17, where z^S=1, z^R=2, z^C=1, δ_1=0.1, δ_2=0.8 and δ_3=0.1, all initial carrier state occupancies (NE_i^0, NE_o^0, NES_i^0, NES_o^0, $NESR_i^0$ and $NESR_o^0$) were set to ten, and initial rate constant values were set to the following values: a_o^0= $9.88 \cdot 10^2$, b_i^0=0.07, b_o^0=1.16, f_i^0=5.78, f_o^0=0.05, g_i^0=5.30, g_o^0=2.13, h_i^0=7.34, h_o^0=0.29, m_i^0=0.17, m_o^0=9.25, n_i^0=17.00 and n_o^0=9.25[VIII]. To study our model system without carrier charge effects, z^C was set to zero and initial values of reorientation rate constants were changed to: a_o^0= $35.55 \cdot 10^2$, b_i^0=0.02, b_o^0=4.16, f_i^0=1.61 and f_o^0=0.18[VIII]. Rate constant a_i was calculated according to Equation 18 to ensure that our model observes the principle of detailed balance. Because rate constants b_i^0 and b_o^0 are not included in Equation 18 (i.e. there are no constraints on them arising from the detailed balance condition), they can be set to any possible value and therefore notably influence transport characteristics. Since b_i^0 and b_o^0 describe reorientation of the carrier loaded with substrate S, their value can either support or inhibit both the leak of S substrate and the co-transport of S and R. For certain values of b_i^0, we even observed antiport of S and R instead of symport. Nevertheless, we managed to find a set of rate constants that allows us to observe reasonable symport of both substrates and, under some conditions, active transport of substrate R.

First of all, we studied the effects of outer substrate S and R concentration on carrier transport (Figure 30 – Figure 32). At a membrane potential of -44 mV (Figure 30), substrate S

[VIII] Rate constant values are rounded to two decimal digits.

started to be transported into the cell as its outer concentration reached the equilibrium value. Active transport of R was observed when c^S_o was sufficiently high to drive R uptake against its concentration gradient. Similarly, outer substrate R concentration also needed to reach a certain value to enable active influx of substrate R. Interestingly, substrate S influx was shown to be c^R_o dependent as well. Its decrease at higher c^R_o values can be explained by the fact that when R concentration outside is high, carrier in an ES_o state starts to prefer substrate R binding before reorientation to the inside with only substrate S bound. At extremely high electrochemical gradients of R directed outwards, both substrates are transported in a thermodynamically passive manner and the carrier acts like an antiport. To summarise, varying both the outer S and R concentrations remarkably changed stoichiometry of the observed S and R co-transport. For example, at high outer R concentrations, both substrates are co-transported together with a stoichiometry 1:1, but when c^R_o=1, S influx exceeds R influx for all studied c^S_o values. The H^+:Fe^{2+} stoichiometry of Nramp2 was described to rise with an increasing electrochemical gradient of protons [34,52] – a similar effect can be observed in Figure 30 a). In Figure 30 b), influx of S approaches a stable value as c^R_o goes to zero. This could represent the uncoupled flux observed for Nramp2 in [35]. Uncoupled S influx diminishes as c^R_o rises and coupled flux (with a stoichiometry of 1:1) becomes dominant.

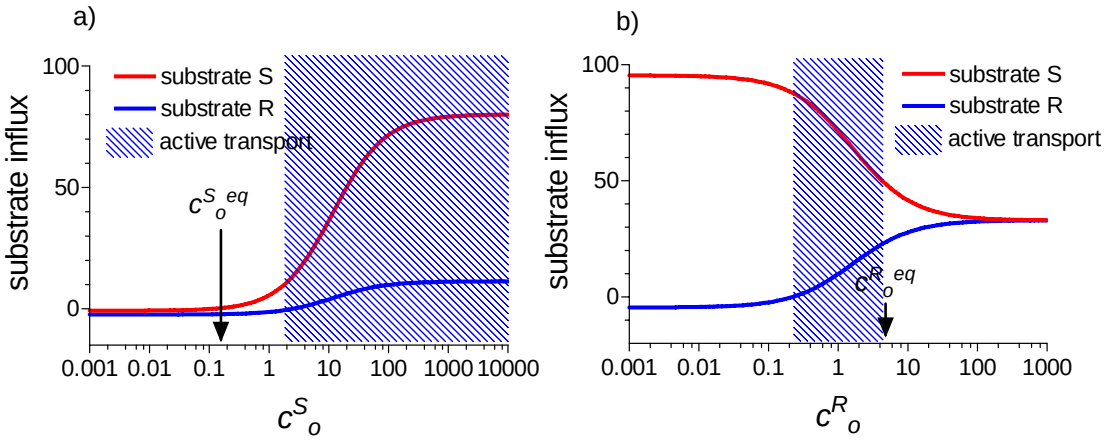

Figure 30 – Influx of substrates S and R vs. concentration of substrate S or R outside the cell (in a logarithmic scale) at a membrane potential of -44 mV. S and R outer equilibrium concentrations and the area where active transport is observed (where substrate R was transported into the cell although $c^R_o < c^{R\,eq}_o$) are marked.

As a next step, concentration effects together with voltage and carrier charge effects were studied (Figure 31 and Figure 32). Both the R influx at negative membrane potential values and R efflux at positive potentials are higher when carrier charge effects are not

considered (except for the membrane potential -80 mV where substrate influx was set by our choice of rate constants to have the same value for both carrier charges). Moreover, a previously described effect of narrowing the voltage range that is optimal for transport by non-zero carrier charge values was observed.

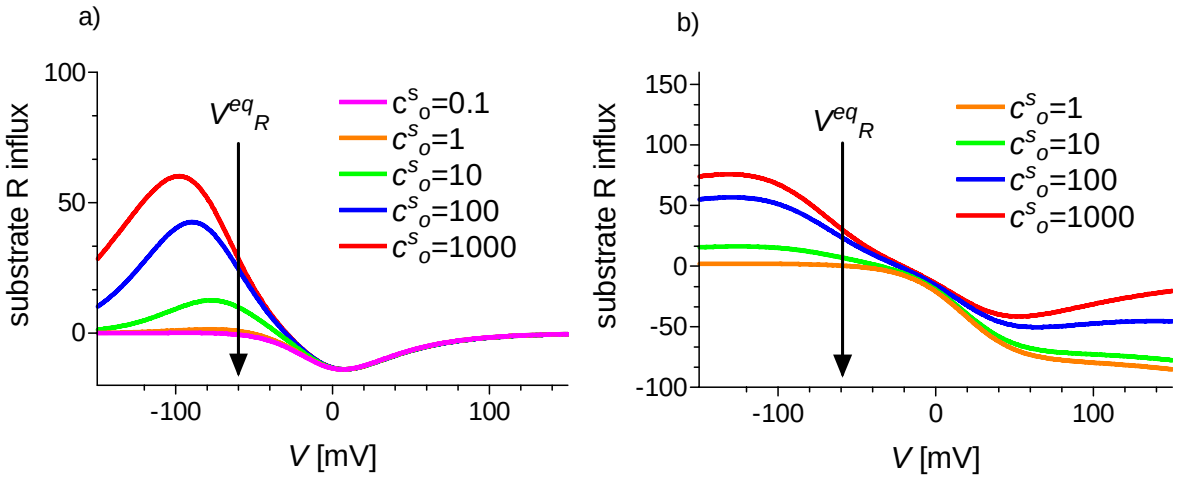

Figure 31 – Voltage dependence of substrate R influx at various S concentrations outside the cell when a) z^C=1 b) z^C=0. Equilibrium membrane potential values for the R substrate, calculated from Equation 18, are marked. For c^S_o>0.1, active transport of substrate R into the cell (positive R influx when $V > V^{eq}_R$) is observed. Generally, R influx is positive at negative membrane potential values and becomes negative when membrane potential is positive. However, at outer S concentrations 1 and less, R efflux is observed even when membrane potential is slightly negative when z^C=1 (Panel a)).

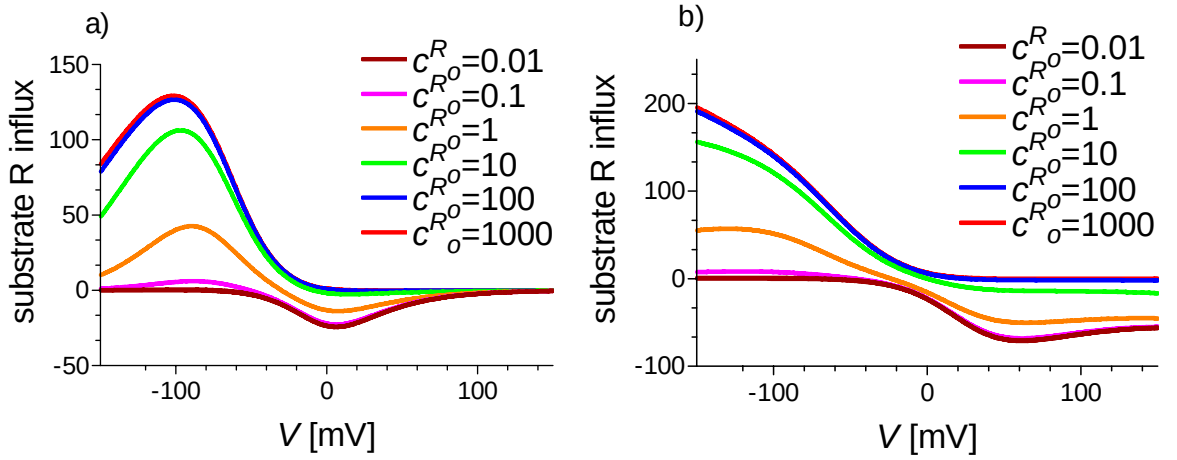

Figure 32 – Voltage dependence of substrate R influx at various R concentrations outside the cell when a) z^C=1 b) z^C=0

The stoichiometry of S and R co-transport for several substrate S and R concentrations is shown in Figure 33. When we look at the voltage dependence of S:R stoichiometry ratio, we see that when the membrane potential changes to more negative values, S:R ratio increases. This phenomenon was measured in *Xenopus* oocytes expressing Nramp2 [34] and described as "proton slip" [45]. The sharp rise of the S:R ratio accompanying membrane potential increase reflects the zero R influx when it would be thermodynamically unfavourable. This situation obviously did not occur in experiments of Chen et al. [34].

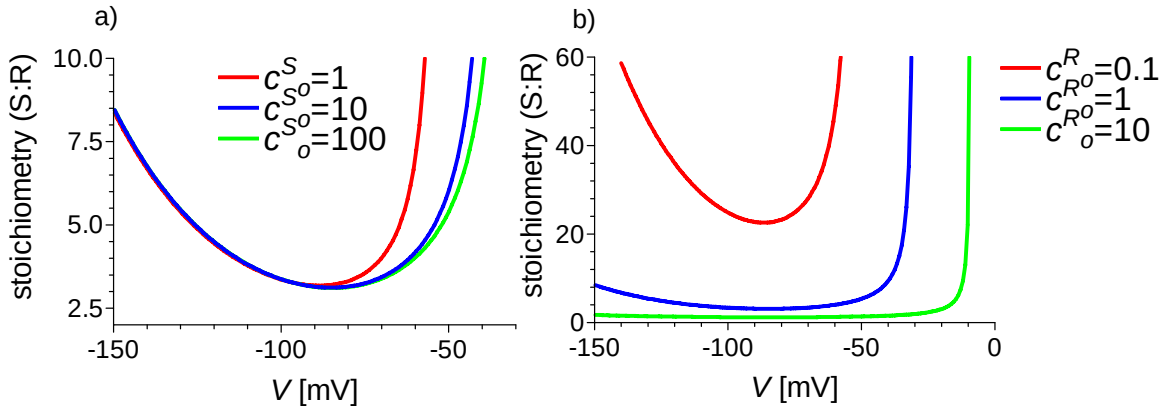

Figure 33 – Stoichiometry of the S and R co-transport when z^C=1 a) for different c^S_o values b) for different c^R_o values

As a next step, we studied carrier charge effects on carrier reorientation in more detail. Curves describing the influence of S influx by carrier charge have exactly the same form as for the electrogenic four-state carrier (Figure 27) which means that negative carrier charge enables influx of a positively charged substrate at positive membrane potential values and positive carrier charge facilitates influx when membrane potential is negative (data not shown). On the other hand, positive values of R influx were observed only for carrier charges from zero to five; for all other carrier charge values, R influx was either negative or almost zero. This is a consequence of our choice of rate constants that were adjusted to allow positive influx of R when z^C=0 and z^C=1; a different choice of rate constants could shift the carrier charge range where positive R influx is observed towards more positive or negative values. In general, increasing the absolute value of carrier charge considerably reduces R influx (or efflux, depending on the membrane potential) (Figure 34).

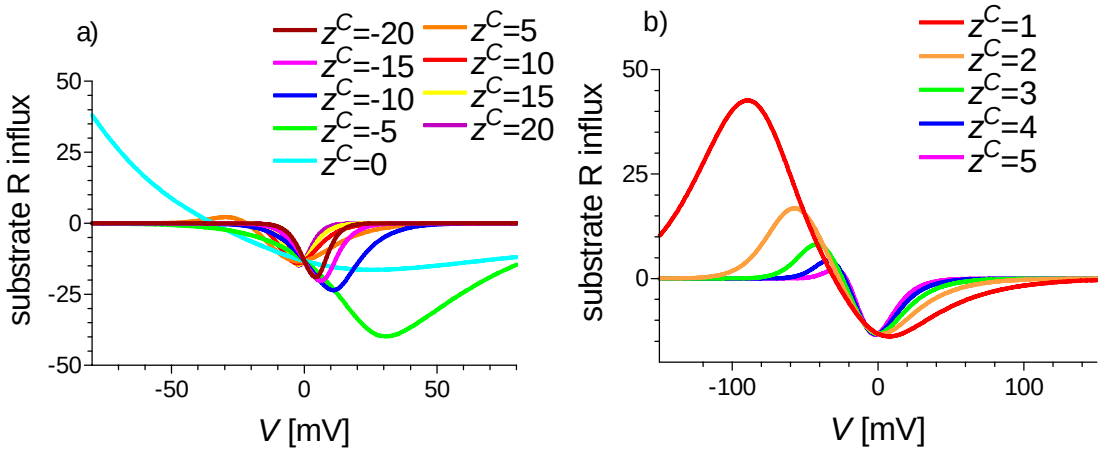

Figure 34 – Voltage and carrier charge effects on R influx

Interestingly, substrate S influx is influenced not only by the charge of substrate S (Figure 35), but also by the charge of the co-transported substrate R (Figure 36). R influx is also greatly influenced by the value of z^S and z^R (data not shown). Such a profound effect of both substrate charges on both substrate fluxes can be explained by the fact that they influence not only the equilibrium condition expressed by Equation 18 but also the final rate constant values according to Equation 17. This affects all carrier state occupancies and therefore also substrate S and R influxes calculated from Equations 19 and 20.

For negative membrane potential values, S influx increases with the increasing value of substrate S or R charge; analogically, it increases with decreasing substrate S or R charge at positive membrane potentials. Generally, the incorporation of carrier charge effects suppress S influx at a given membrane potential; this is most evident at extremely negative membrane potential values. Positive carrier charge supports efflux of negatively charged substrates at negative membrane potential values because it lowers the relative negative charge sensed by the carrier during reorientation.

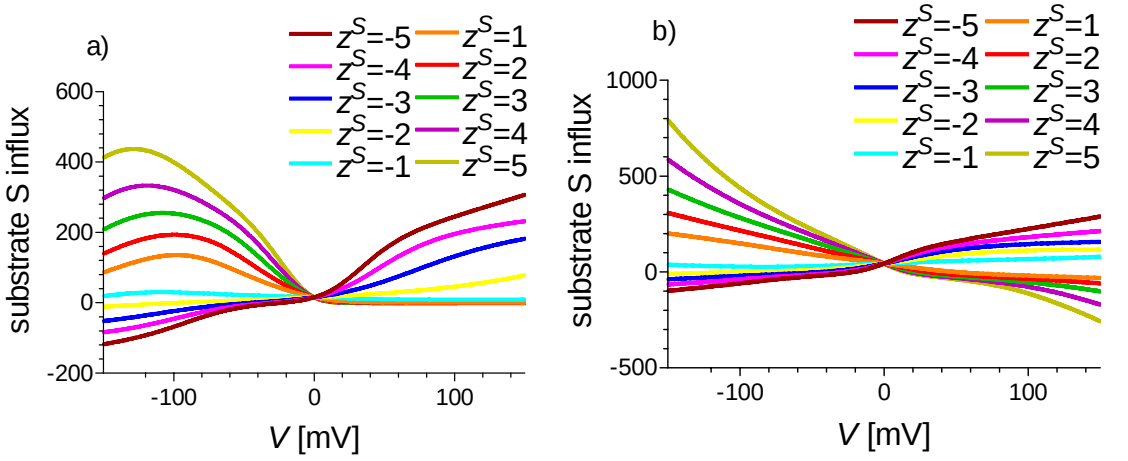

Figure 35 – Voltage and substrate S charge effects on substrate S influx when a) z^C=1 b) z^C=0

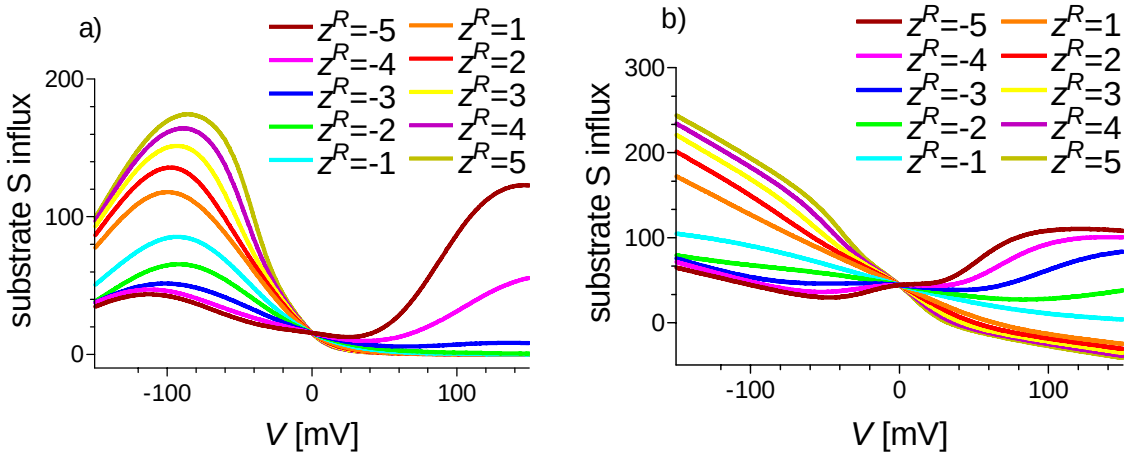

Figure 36 – Voltage and substrate R charge effects on substrate S influx when a) z^C=1 b) z^C=0

Effect of the membrane potential fraction δ_2 on substrate R transport was studied for both the charged and uncharged six-state carrier (Figure 37). Fluxes observed at a certain voltage value when z^C=0 are generally higher than fluxes observed at the same voltage when z^C=1, and the voltage range where substrate influx is different from zero is wider when carrier charge effects are not considered. Similarly to the four-state carrier model, the optimal value of δ_2 for which the highest R influx is observed depends on the studied voltage range. Therefore, substrate influx is not always highest when δ_2=1 i.e. when the effect of voltage on carrier reorientation is maximal.

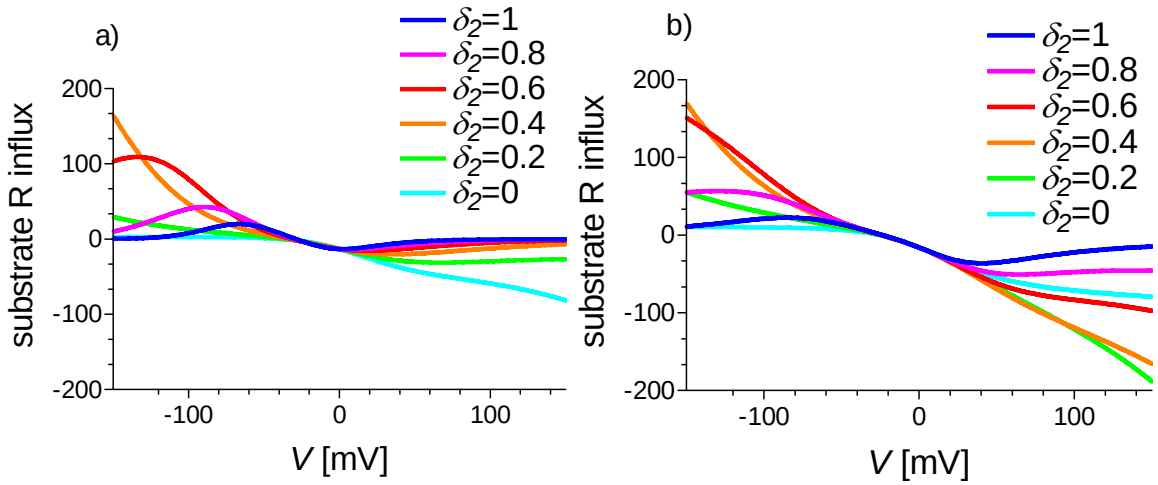

Figure 37 – Influx of substrate R vs. membrane potential for different values of δ_2 when a) z^C=1 b) z^C=0. Parameters δ_1 and δ_3 were chosen to equal each other and obey Equation 7. The optimal δ_2 value for which substrate R influx is maximal depends on the membrane potential range studied. For example, when z^C=1 and the applied membrane potential lies between -48 mV and 0 mV, influx of substrate R reaches its maximal value when δ_2=1. However, within the voltage range from -71 mV to -48mV, influx reaches its highest possible value when δ_2=0.8, etc.

Finally, we can compare some of the transport characteristics of a four-state and a six-state carrier. However, this comparison is only approximate because we used a different set of rate constants to describe each of the models. Nevertheless, we can observe a very similar c^S_o and z^C dependence of substrate S influx in both carrier types. Curves describing substrate S dependence on z^S have a similar behaviour for both carrier models, but when z^C=0, this curves are not so symmetric for the six-state carrier as for the four-state one. In addition, S influx via the six-state carrier depends also on the concentration and charge of the co-transported substrate R.

3.2.4 Voltage effects on the MntH transport protein

The eight state MntH model suggested in [1] (Figure 9) was simulated according to Equation 21, and the voltage dependence of all rate constants was incorporated using Equation 22. Initial rate constant values were set as following: a^0=2.56·10^7, b^0=98.27, c^0=5.10·10^8, d^0=92.50, f^0=3.76, g^0=4.23·10^7, h^0=3.18, i^0=7.19, j^0=67.63, k^0=2.70·10^8, l^0=0.26, m^0=1.34·10^8, β^0=0.29, γ^0=4.52·10^6, δ^0=9.21·10^{-6}, ε^0=3.43·10^6, ζ^0=2.35·10^{-6}, η^0=1.20·10^8

and θ^0=2.46·10^{-7} [IX]. α was calculated from Equation 23 to ensure that the principle of detailed balance is observed. Carrier charge was calculated according to the actual *pH* outside the cell using a calibration curve created in CLC protein workbench for a sequence of *E. coli* MntH[X]. In most of our simulations, pH_i=7.6, pH_o=7, z^C=10.26, and Fe^{2+} concentration inside the cell was 100 times higher than the concentration outside ($c^{Fe}{}_i$=10^{-6} and $c^{Fe}{}_o$=10^{-8}). Initial state occupancies were set to the following values: NE_i=NE_o=10, NES_i=NES_o=13, NER_i=NER_o=2 and $NESR_i$=$NESR_o$=25.

The goal of our simulations was to observe active Fe^{2+} transport into the cell driven by the H^+ influx and, under favourable conditions, also uncoupled Fe^{2+} or H^+ fluxes described in [1]. We succeeded in simulating both the proton slip at low pH_o values and the H^+ uncoupled Fe^{2+} influx at high pH_o (Figure 38 b)). However, we did not see the effect of active Fe^{2+} transport caused by H^+ uptake into the cell (Figure 38 a)) – Fe^{2+} influx became positive at a $c^{Fe}{}_o$ concentration higher than $c^{Fe}{}_o{}^{eq}$. Moreover, H^+ influx was very small for high $c^{Fe}{}_o$ values where high Fe^{2+} influx was observed. This non-standard behaviour of Fe^{2+} influx probably occurred due to the addition of two more carrier states describing uncoupled Fe^{2+} influx to the carrier scheme.

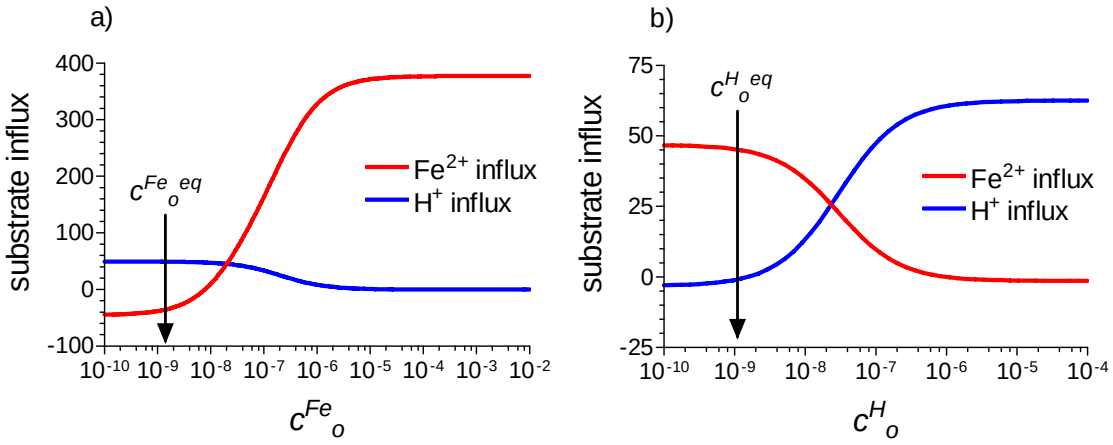

Figure 38 – The dependence of MntH-mediated transport on the concentration of both substrates at -80 mV. a) Fe^{2+} and H^+ influx vs. outer Fe^{2+} concentration b) Fe^{2+} and H^+ influx vs. outer H^+ concentration. Fe^{2+} and H^+ concentrations inside the cell are $c^{Fe}{}_i$=10^{-6} and $c^{H}{}_i$=2.5·10^{-8} (pH_o=7.6). Equilibrium Fe^{2+} and H^+ concentrations are marked when applicable.

[IX] Rate constant values are rounded to two decimal digits.
[X] 1.1.1CLC Protein Workbench – www.clcbio.com

As a next step, we varied outer *pH* and appropriately changed the carrier charge for each value (Figure 39). Higher pH_o does not only increase Fe^{2+} influx and decrease H^+ influx as discussed above, but also shifts the optimal voltage range where substrate fluxes are positive to more negative values.

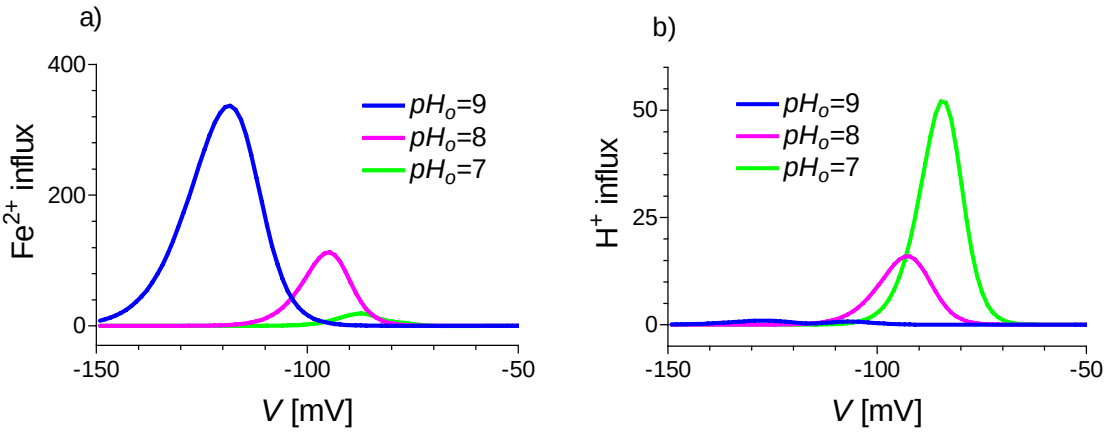

Figure 39 – Voltage and pH_o effects on a) Fe^{2+} influx b) H^+ influx in a general eight-state carrier. Carrier charge was appropriately changed for each pH_o value.

For the purpose of exploring carrier charge effects on Fe^{2+} and H^+ transport, a new set of initial reorientation rate constant values was created to describe the carrier when carrier charge effects are neglected: β^0=14.66·10^4, γ^0=8.95, δ^0=4.65, ε^0=6.79, ζ^0=1.19, η^0=2.38·10^2 and θ^0=0.12[XI]. Results obtained with this model system were then compared to results obtained when original rate constants were used and carrier charge was set to a value corresponding to the *pH* outside the cell (Figure 40). Carrier charge effects dramatically changed the voltage range where Fe^{2+} and H^+ influx can be observed, and did not allow any efflux at positive membrane potential values. When z^C=0, high values of Fe^{2+} and H^+ influxes were observed at very low membrane potential values and a reasonable efflux occurred at positive membrane potential values. Independent of z^C, H^+ influx gets higher with decreasing outer Fe^{2+} concentration. This means that H^+ influx through the MntH carrier is uncoupled from Fe^{2+} at low $c^{Fe}{}_o$ values as discussed in [1] for both carrier charges (z^C=10.26 and z^C=0).

[XI] Rate constant values are rounded to two decimal digits.

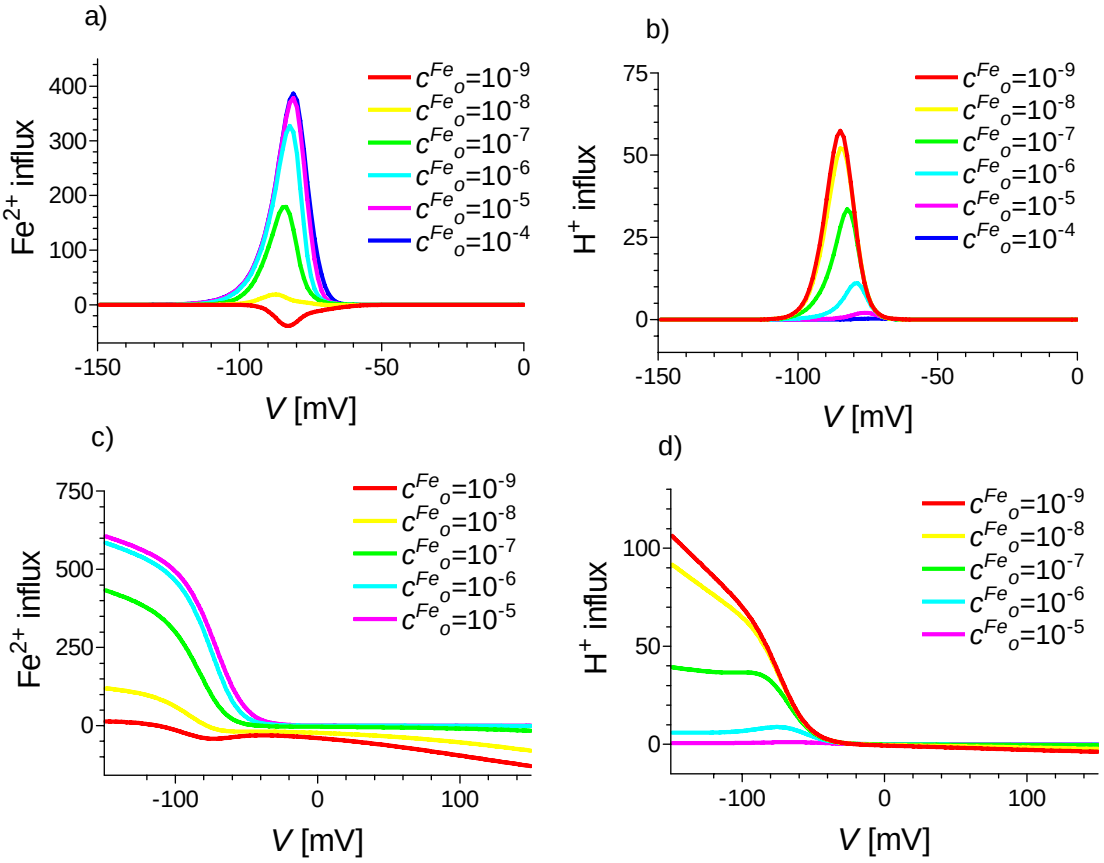

Figure 40 – Voltage dependence of Fe^{2+} influx for different values of c^{Fe}_o when a) z^C=10.26 c) z^C=0; and voltage dependence of H^+ influx for different values of c^{Fe}_o when b) z^C=10.26 d) z^C=0. c^{Fe}_i=10^{-6}, c^H_i=$2.5 \cdot 10^{-8}$ and c^H_o=10^{-7}.

To summarise, although we did not manage to simulate active symport of Fe^{2+} caused by H^+ influx, we succeed in modelling some of the leakage effects described in [1]. The eight-state carrier model is quite difficult to simulate as it is described by a large number of model parameters that have to be set properly to obtain reasonable results. In addition, the principle of detailed balance does not include Fe^{2+} concentration and charge as well as reorientation rate constants γ, δ, ε and ζ (see Equation 23); these can therefore be set to any selected values. Incorporating the possibility that protons are able to bind to the enzyme state with bound metal ions would lead to an even bigger increase of model parameters that can be freely set because the carrier scheme would have a cubic shape, and reorientation rate constants as well as the concentration and charge of both substrates would not affect the principle of detailed balance. It seems that when we want to simulate the MntH carrier, we have to choose either

a simple and easily adjustable model or a more complex model that can describe some special transport characteristics but is more complicated to simulate.

To obtain theoretical results that could really be comparable to experimental observations, we would need to have more detailed knowledge of the approximate rate constant values and also of substrate concentrations that are likely to occur inside and outside a cell. Despite of these limitations, using the six-state and eight-state carrier, models, we managed to describe some of the characteristics of MntH-mediated transport that were observed experimentally such as uncoupled fluxes of protons or metal ions and variable co-transport stoichiometry. This is certainly a great success considering that we had almost no clue how to set rate constants and other model parameters to reasonable values. Another problem in comparing our simulated data with experimental results arises from the fact that it is not clear whether metal concentrations measured in cells refer to the concentration of free or chelatated metal ions. Therefore, it can be hard to distinguish the exact amount of metal ions transported via MntH.

4 Conclusions

4.1 Membrane potential of *E.coli* cells and metal ion transport mediated by MntH

The overall goal of our work was to study transport characteristics of the bacterial MntH protein, a member of a large conserved Nramp protein family that co-transports divalent metal ions and protons. Experimentally, we successfully studied the effects of *MNTH* overexpression and electrogenic metal ion transport via the MntH protein on cell membrane potential using the membrane potential-sensitive fluorescent probe diS-C_3(3). Expression of *MNTH* was found to increase staining by the probe, suggesting that cells containing MntH are hyperpolarised. The reason of this membrane potential shift is not clear. One possible explanation would be that the MntH-mediated proton flux is compensated by a flow of other ion that lowers pH_i but not the membrane potential. This counter-flux (if there is any) could be mediated by MntH, or other transport protein.

Under some experimental conditions, membrane potential depolarisation was observed in EcoliA and N401G cells upon the addition of $MnCl_2$ and $CdCl_2$. Because membrane potential of pBAD cells (negative control) and D34G cells (mutant strain with non-functional MntH) remained unchanged upon the addition of metal ions, we can conclude that membrane potential shifts observed in EcoliA and N401G cells are a result of Mn^{2+} and Cd^{2+} transport

into the cell. In *pHLUORIN* expressing cells, an increase in the apparent intracellular *pH* value was observed upon the addition of diS-C_3(3). pH_i value decreased after the addition of divalent metals in transport-competent mutant N401G, but not in inactive D34G. This suggests that the simultaneous measurements of pH_i and membrane potential can be performed, but a new calibration of internal *pH* in the presence of diS-C_3(3) has to be done to interpret pH_i changes quantitatively.

4.2 Transport kinetics of four-, six- and eight-state carriers

We successfully simulated kinetic equations describing a general four-, six- and eight-state carrier model with voltage dependent rate constants. Because the traditional approximation considering the carrier to be simple[XII] and symmetric[XIII] has been recently frequently questioned, we performed most of our simulations on a general carrier model with no other restrictions on the rate constant values than the principle of detailed balance.

Using uniporter and symporter carrier models, we concentrated on the effects of voltage and carrier charge, but explored also the influence of rate constant values, substrate concentration and charge. We proved that, due to the carrier charge and voltage dependence of carrier reorientation steps, even an electroneutral uniporter can be greatly influenced by the value and time course of applied membrane potential. Oscillating membrane fields that can arise for example due to the activity of ion channels, membrane pumps or excitable cells were shown to greatly influence substrate flux even when the carrier is electroneutral. These effects were recently further explored experimentally using voltage clamp experiments together with other transport techniques in the laboratory of Dr. Bernhard Schmitt at the University of Otago, but up to now, no results of these experiments were published. For electrogenic carriers, voltage effects are more complicated as they include also the influence of substrate charge on all transport steps.

One of our aims was to study how transport kinetics is influenced by the fact that during carrier reorientation, several of its charged residues are moving in the electric field. In all studied carrier models, incorporating carrier charge effects influenced mainly the voltage range where transport can be observed. For a four-state electroneutral carrier, substrate flux was smaller when carrier charge and voltage had non-zero values then when carrier charge or voltage equalled zero. In the more complicated cases of an electrogenic four- and six-state

[XII] Substrate binding and releasing steps are much faster than reorientation steps
[XIII] Reorientation rate constants are the same for both empty and loaded carriers

carrier model, also the maximal possible value of substrate influx was changing with different carrier charge.

The main goal of our simulations was to study MntH-mediated symport. MntH has quite unusual transport properties as it is not common for the co-transport of a positively charged substrate to be driven by the influx of a positively charged ion. We succeeded in finding a set of rate constants that enabled us to simulate active substrate influx via a six-state symporter that can be regarded as a simplified scheme of the MntH carrier. Stoichiometry of the observed co-transport varied greatly with applied membrane potential and outer concentration of substrates – a similar effect was experimentally described in [34,52]. At a low concentration of the co-transported metal ion, we simulated uncoupled influx of protons that was measured by Gunshin et al. [35].

The six-state scheme is sufficient to describe proton leak, but does not explain H^+-uncoupled metal uniport. Therefore, we also simulated the eight-state carrier model designed specially to explain transport properties of Nramp family proteins. We were successful in modelling the proton leak at low pH_o values and the metal ion leak at high pH_o; these effects were described in [1]. However, the number of model parameters that have to be adjusted is increasing with the increasing complexity of the carrier scheme. Therefore, the eight-state carrier model gives us a lot of freedom in varying carrier transport properties and it is not trivial to set all model parameters to reasonable values. In a four-state carrier, all rate constants and substrate charges and concentrations are bound by the principle of detailed balance. Although increasing the complexity of the carrier model leads to a better description of symport properties, it increases the number of parameters that can be set freely (i.e. that are not bound by the principle of detailed balance) but have to be adjusted to reasonable values so as to simulate experimentally observed transport effects (positive substrate influx at physiological membrane potential values or secondary active transport, for example).

To conclude, we managed to find reasonable model parameters which enabled us to qualitatively describe some of the MntH-mediated transport properties that were observed experimentally. To improve our simulations, it would be useful to have more detailed information about real values of rate constants and other model parameters.

5 References

1. B.Mackenzie, M.L.Ujwal, M.H.Chang, M.F.Romero, and M.A.Hediger, Divalent metal-ion transporter DMT1 mediates both H^+-coupled Fe^{2+} transport and uncoupled fluxes, Pflugers Arch. 451 (2006) 544.

2. B.Alberts, A.Johnson, J.Lewis, M.Raff, K.Roberts, and P.Walter, Molecular Biology of the Cell 4th Ed., Garland Science, New York and London, 2002.

3. L.J.Van Winkle, Biomembrane Transport, Academic Press, San Diego, 1999.

4. P.L.Yeagle, The Structure of Biological Membranes, CRC press, 2004.

5. G.J.Siegel, R.W.Albers, D.L.Price, and S.Brady, Basic Neurochemistry - Molecular, Cellular and Medical Aspects, Elsevier Science, 2005.

6. P.Lauger, Dynamics of ion transport systems in membranes, Physiol. Rev. 67 (1987) 1296.

7. T.F.Weiss, Cellular Biophysics, Massachusetts Institute of Technology, 1996.

8. D.Sanders, U.P.Hansen, D.Gradmann, and C.L.Slayman, Generalized kinetic analysis of ion-driven cotransport systems: A unified interpretation of selective ionic effects on michaelis parameters, Journal of Membrane Biology 77 (1983) 123.

9. A.Su, S.Mager, S.L.Mayo, and H.A.Lester, A multi-substrate single-file model for ion-coupled transporters, Biophys. J. 70 (1996) 762.

10. B.Robertson and R.D.Astumian, Kinetics of a multistate enzyme in a large oscillating field, Biophys. J. 57 (1990) 689.

11. H.V.Westerhoff, T.Y.Tsong, P.B.Chock, Y.D.Chen, and R.D.Astumian, How enzymes can capture and transmit free energy from an oscillating electric field, Proceedings of the National Academy of Sciences of the United States of America 83 (1986) 4734.

12. L.W.Horn, A Novel Method for the Observation of Membrane Transporter Dynamics, 1993, pp.281-289.

13. W.F.Boron and E.L.Boulpaep, Medical Physiology, W.B. Saunders Company, 2002.

14. S.H.Wright, Generation of resting membrane potential, Adv. Physiol. Educ. 28 (2004) 139.

15. D.Purves, Neuroscience, Sinauer Associates, Inc., 2007.

16. C.M.Armstrong, Channels and Pumps Early in Evolution, in: F.V.Sepúlveda and F.Bezanilla (Eds.), Pumps, transporters, and ion channels, Centro de Estudios Cientificos, Kluwer Academic/Plenum publishers, New York, 2005, pp.1-10.

17. H.A.Pohl, in: W.R.Adey and A.F.Laurence (Eds.), Nonlinear Electrodynamics in biological systems, Plenum, New York, 1984, pp.3-22.

18. R.D.Astumian, Effects of time-dependent electric fields on membrane transport, Biophys. J. 64 (1993) 7.

19. P.E.Rapp, Why are so many biological systems periodic?, Prog. Neurobiol. 29 (1987) 261.

20. D.S.Liu, R.D.Astumian, and T.Y.Tsong, Activation of Na+ and K^+ pumping modes of (Na,K)-ATPase by an oscillating electric field, J Biol Chem. 265 (1990) 7260.

21. E.H.Serpersu and T.Y.Tsong, Activation of electrogenic Rb^+ transport of (Na,K)-ATPase by an electric field, J Biol Chem. 259 (1984) 7155.

22. R.D.Astumian, P.B.Chock, T.Y.Tsong, Y.D.Chen, and H.V.Westerhoff, Can free energy be transduced from electric noise?, Proceedings of the National Academy of Sciences of the United States of America 84 (1987) 434.

23. T.D.Xie, Y.Chen, P.Marszalek, and T.Y.Tsong, Fluctuation-driven directional flow in biochemical cycle: further study of electric activation of Na,K pumps, Biophys. J. 72 (1997) 2496.

24. N.Nelson, Metal ion transporters and homeostasis, EMBO J. 18 (1999) 4361.

25. Y.Nevo and N.Nelson, The NRAMP family of metal-ion transporters, Biochim. Biophys. Acta 1763 (2006) 609.

26. M.D.Fleming, C.C.Trenor, III, M.A.Su, D.Foernzler, D.R.Beier, W.F.Dietrich, and N.C.Andrews, Microcytic anaemia mice have a mutation in Nramp2, a candidate iron transporter gene, Nat. Genet. 16 (1997) 383.

27. K.M.Papp, D.Kehres, and M.Maguire, Manganese and Iron Transport by Prokaryotic Nramp Family Transporters, in: M.Cellier and P.Gros (Eds.), The Nramp Family, Kluver Academic/Plenum Publishers, New York, 2004, pp.154-172.

28. P.Courville, R.Chaloupka, and M.F.M.Cellier, Recent progress in structure-function analyses of Nramp proton-dependent metal-ion transporters, Biochem. Cell Biol. 84 (2006) 960.

29. D.G.Kehres, A.Janakiraman, J.M.Slauch, and M.E.Maguire, Regulation of *Salmonella enterica* serovar Typhimurium mntH transcription by H_2O_2, Fe^{2+}, and Mn^{2+}, J. Bacteriol. 184 (2002) 3151.

30. D.W.Christianson, Structural chemistry and biology of manganese metalloenzymes, Prog. Biophys. Mol. Biol. 67 (1997) 217.

31. R.M.Tsolis, A.J.Baumler, and F.Heffron, Role of *Salmonella typhimurium* Mn-superoxide dismutase (SodA) in protection against early killing by J774 macrophages, Infect. Immun. 63 (1995) 1739.

32. D.G.Kehres, M.L.Zaharik, B.B.Finlay, and M.E.Maguire, The NRAMP proteins of Salmonella typhimurium and Escherichia coli are selective manganese transporters involved in the response to reactive oxygen, Mol. Microbiol. 36 (2000) 1085.

33. M.F.Cellier, G.Prive, A.Belouchi, T.Kwan, V.Rodrigues, W.Chia, and P.Gros, Nramp defines a family of membrane proteins, Proc. Natl. Acad. Sci. U. S. A 92 (1995) 10089.

34. X.Z.Chen, J.B.Peng, A.Cohen, H.Nelson, N.Nelson, and M.A.Hediger, Yeast SMF1 mediates H^+-coupled iron uptake with concomitant uncoupled cation currents, J. Biol. Chem. 274 (1999) 35089.

35. H.Gunshin, B.Mackenzie, U.V.Berger, Y.Gunshin, M.F.Romero, W.F.Boron, S.Nussberger, J.L.Gollan, and M.A.Hediger, Cloning and characterization of a mammalian proton-coupled metal-ion transporter, Nature 388 (1997) 482.

36. H.Makui, E.Roig, S.T.Cole, J.D.Helmann, P.Gros, and M.F.Cellier, Identification of the Escherichia coli K-12 Nramp orthologue (MntH) as a selective divalent metal ion transporter, Mol. Microbiol. 35 (2000) 1065.

37. E.Pinner, S.Gruenheid, M.Raymond, and P.Gros, Functional complementation of the yeast divalent cation transporter family *SMF* by *NRAMP2,* a member of the mammalian natural resistance-associated macrophage protein family, J. Biol. Chem. 272 (1997) 28933.

38. E.Richer, P.Courville, and Cellier M.F.M., Evolutionary Analysis of Nramp Family, in: M.Cellier and P.Gros (Eds.), The Nramp family, Landes Bioscience, Georgetown, TX, 2003.

39. M.F.Cellier, I.Bergevin, E.Boyer, and E.Richer, Polyphyletic origins of bacterial Nramp transporters, Trends Genet. 17 (2001) 365.

40. P.Courville, R.Chaloupka, F.Veyrier, and M.F.Cellier, Determination of Transmembrane Topology of the Escherichia coli Natural Resistance-associated Macrophage Protein (Nramp) Ortholog, J. Biol. Chem. 279 (2004) 3318.

41. F.Supek, L.Supekova, H.Nelson, and N.Nelson, A yeast manganese transporter related to the macrophage protein involved in conferring resistance to mycobacteria, Proc. Natl. Acad. Sci. U. S. A 93 (1996) 5105.

42. A.Sacher, A.Cohen, and N.Nelson, Properties of the mammalian and yeast metal-ion transporters DCT1 and Smf1p expressed in Xenopus laevis oocytes, J. Exp. Biol. 204 (2001) 1053.

43. E.Luk, L.Jensen, and V.C.Culotta, The Role of Yeast Nramp Metal Transporter in Manganese and Iron Homeostasis, in: M.Cellier and P.Gros (Eds.), The Nramp Family, Kluver Academic/Plenum Publishers, New York, 2004.

44. M.E.Portnoy, X.F.Liu, and V.C.Culotta, *Saccharomyces cerevisiae* expresses three functionally distinct homologues of the Nramp family of metal transporters, Mol. Cell. Biol. 20 (2000) 7893.

45. N.Nelson, A.Sacher, and H.Nelson, The significance of molecular slips in transport systems, Nat. Rev. Mol Cell Biol 3 (2002) 876.

46. A.Cohen, H.Nelson, and N.Nelson, Metal-Ion Transporters: From Yeast to Human Diseases, in: M.Cellier and P.Gros (Eds.), The Nramp Family, Kluver Academic/Plenum Publishers, New York, 2004.

47. S.Vidal, M.L.Tremblay, G.Govoni, S.Gauthier, G.Sebastiani, D.Malo, E.Skamene, M.Olivier, S.Jothy, and P.Gros, The Ity/Lsh/Bcg locus: natural resistance to infection with intracellular parasites is abrogated by disruption of the Nramp1 gene, J. Exp. Med. 182 (1995) 655.

48. S.Gruenheid, E.Pinner, M.Desjardins, and P.Gros, Natural resistance to infection with intracellular pathogens: the Nramp1 protein is recruited to the membrane of the phagosome, J. Exp. Med. 185 (1997) 717.

49. G.Govoni, S.Gauthier, F.Billia, N.N.Iscove, and P.Gros, Cell-specific and inducible Nramp1 gene expression in mouse macrophages in vitro and in vivo, J. Leukoc. Biol. 62 (1997) 277.

50. M.F.Cellier, C.Shustik, W.Dalton, E.Rich, J.Hu, D.Malo, E.Schurr, and P.Gros, Expression of the human NRAMP1 gene in professional primary phagocytes: studies in blood cells and in HL-60 promyelocytic leukemia, J. Leukoc. Biol. 61 (1997) 96.

51. A.C.Chua and E.H.Morgan, Effects of iron deficiency and iron overload on manganese uptake and deposition in the brain and other organs of the rat, Biol. Trace Elem. Res. 55 (1996) 39.

52. Y.Nevo and N.Nelson, The mutation F227I increases the coupling of metal ion transport in DCT1, J. Biol. Chem. 279 (2004) 53056.

53. D.Agranoff, I.M.Monahan, J.A.Mangan, P.D.Butcher, and S.Krishna, Mycobacterium tuberculosis expresses a novel pH-dependent divalent cation transporter belonging to the Nramp family, J. Exp. Med. 190 (1999) 717.

54. M.L.Zaharik, V.L.Cullen, A.M.Fung, S.J.Libby, S.L.Kujat Choy, B.Coburn, D.G.Kehres, M.E.Maguire, F.C.Fang, and B.B.Finlay, The Salmonella enterica Serovar Typhimurium Divalent Cation Transport Systems MntH and SitABCD Are Essential for Virulence in an Nramp1G169 Murine Typhoid Model, Infect. Immun. 72 (2004) 5522.

55. J.D.Helmann, Regulation of Bacterial MntH Genes, in: Cellier M.F.M. and P.Gros (Eds.), The Nramp Family, Springer, 2004, pp.146-153.

56. J.Vecer, P.Herman, and A.Holoubek, Diffusion membrane potential in liposomes: setting by ion gradients, absolute calibration and monitoring of fast changes by spectral shifts of diS-C_3(3) fluorescence maximum, BBA-Biomembranes 1325 (1997) 155.

57. D.Gaskova, A.DeCorby, and B.D.Lemire, DiS-C_3(3) monitoring of in vivo mitochondrial membrane potential in C. elegans, Biochem. Biophys. Res. Commun. 354 (2007) 814.

58. L.Maresova, S.Muend, Y.Q.Zhang, H.Sychrova, and R.Rao, Membrane Hyperpolarization Drives Cation Influx and Fungicidal Activity of Amiodarone, J. Biol. Chem. 284 (2009) 2795.

59. D.Gaskova, R.Cadek, R.Chaloupka, J.Plasek, and K.Sigler, Factors underlying membrane potential-dependent and -independent fluorescence responses of potentiometric dyes in stressed cells: diS-C_3(3) in yeast, Biochim. Biophys. Acta 1511 (2001) 74.

60. A.Kotyk, K.Janacek, and J.Koryta, Biophysical Chemistry of Membrane Functions, John Wiley & Sons, 1988.

61. R.Chaloupka, P.Courville, F.Veyrier, B.Knudsen, T.A.Tompkins, and M.F.Cellier, Identification of functional amino acids in the Nramp family by a combination of evolutionary analysis and biophysical studies of metal and proton cotransport in vivo, Biochemistry 44 (2005) 726.

62. P.Courville, E.Urbankova, C.Rensing, R.Chaloupka, M.Quick, and M.Cellier, Solute Carrier 11 Cation Symport Requires Distinct Residues in Transmembrane Helices 1 and 6, J. Biol. Chem. 283 (2008) 9651.

List of abbreviations

ADP – adenosine diphosphate

ATP – adenosine triphosphate

E. coli – Escherichia coli

GFP – Green Fluorescent Protein

MntH – Manganese transporter H^+-dependent

Nramp – Natural resistance-associated macrophage proteins

TM – transmembrane

Me^{2+} – divalent metal ion

pH_i – intracellular *pH*

pH_o – extracellular *pH*